---

**Article:**
Probert, Matthew Ian James orcid.org/0000-0002-1130-9316 and Hopkinson, Aaron Russell (2018) Quantum diffusion of H/D on Ni(111)—A partially adiabatic centroid MD study. Journal of Chemical Physics. 102339. pp. 1-18. ISSN 1089-7690

https://doi.org/10.1063/1.5004801

---

# Quantum Diffusion of H/D on Ni(111) – a Partially-Adiabatic Centroid MD Study

A.R. Hopkinson* and M.I.J. Probert†
*Department of Physics, University of York, Heslington, York, YO10 5DD, United Kingdom*

We present the results of a theoretical study of H/D diffusion on a Ni(111) surface at a range of temperatures, from 250 K to 75 K. The diffusion is studied using both classical molecular dynamics, and the partially-adiabatic centroid molecular dynamics method. The calculations are performed with the hydrogen (or deuterium) moving in 3D across a static nickel surface using a novel Fourier interpolated potential energy surface which has been parameterized to density functional theory calculations. The results of the classical simulations are that the calculated diffusion coefficients are far too small and with too large a variation with temperature compared with experiment. In contrast, the quantum simulations are in much better agreement with experiment, and show that quantum effects in the diffusion of hydrogen are significant at all temperatures studied. There is also a cross-over to a quantum-dominated diffusive regime for temperatures below $\sim 150$ K for hydrogen and $\sim 85$ K for deuterium. The quantum diffusion coefficients are found to accurately reproduce the spread in values with temperature, but with an absolute value that is a little high compared with experiment.

## I. INTRODUCTION

The diffusion of hydrogen in metals have been studied for a long time. In an early study by Graham[1], it was discovered that hydrogen rapidly diffused through palladium. Since then, many other studies have determined the diffusive properties of hydrogen through a wide variety of metal systems[2]. It has long been known that hydrogen diffusion plays an important role in the embrittlement of metals[3] (particularly steel) which can therefore cause metallic structures/components to fail. One recent prominent example of structural steel failure, which has been attributed to environmental hydrogen embrittlement, was the failure of a number of anchor rods used to support part of the San Francisco-Oakland Bay bridge, only 2 weeks after installation, in 2013[4].

In order to reduce the effects of hydrogen diffusion, it is important to understand the mechanism of diffusion (both classical and quantum) and the effect of potential trapping sites (grain boundaries, defects, interfaces, etc). Whilst classical diffusion is expected to be the dominant mechanism at room temperature and above, quantum diffusion may still play an important role due to the light mass of hydrogen, which can display quantum behaviour at temperatures considerably greater than for other elements[5].

The direct experimental study of hydrogen diffusion is very difficult, but recently there has been significant progress in developing methods to study hydrogen diffusion on high quality metal surfaces. At a surface, the role of quantum processes can be enhanced with respect to the bulk. One system that has been studied by various techniques is that of hydrogen on the Ni(111) surface. It has been experimentally observed that there is evidence of quantum diffusion on the surface of nickel even at relatively high temperatures (with transitions to the quantum regime around 100 K to 125 K)[6–8]. One experimental group[8] has reported that the diffusion rate of hydrogen on nickel may vary by as many as 8 orders of magnitude over a relatively small temperature range (65 K to 240 K) with around 3 orders of magnitude variation below the transition temperature to quantum diffusion. Other studies[6,7] show a change of 1-2 orders of magnitude above the transition temperature and very little variation below it. In short, the experiments are very difficult and there is little consensus in the results.

In recent years, a promising new experimental technique, based on the method of helium spin-echo interferometry, has been developed by Jardine *et al*[9,10]. This technique allows for the accurate measurement of fast diffusive dynamics across surfaces at previously inaccessible length and time scales, and has already been successfully used to characterise the diffusion of hydrogen across Pt and Ru surfaces[11,12]. In addition to these studies, the same experimental group have also gathered data on the diffusion of both hydrogen and deuterium across the nickel (111) surface — these results have suggested diffusion rates which are significantly faster than previously reported (preliminary results suggesting diffusion rates of $\sim 10^{-6}$ to $10^{-7}$ cm$^2$/s across a temperature range of 250 K to 125 K, and transition temperatures of approximately 170 K)[13]. The difference between the newer helium spin-echo experimental results, and the older ones mentioned above, are suspected to be a consequence of the difficulty in tracking the fast adsorbate at the time scales required to accurately determine the diffusion rates.

The aim of this work is to use partially adiabatic centroid molecular dynamics[14–16] (a path integral molecular dynamics (PIMD) based method) in order to directly simulate the diffusion of hydrogen and deuterium on the Ni(111) surface. PIMD-based methods are chosen as an efficient method to include the dominant quantum and classical processes involved in diffusion. Whilst a fully *ab initio* approach would be ideal, the computational cost is too high, and so we present results using a potential energy surface based approach which vastly reduces the

computational resources required to study this problem without sacrificing accuracy.

## II. METHOD

The diffusion of an adsorbate is sensitive to the energy barriers which are encountered as it moves across the surface. It is therefore crucially important that the underlying interactions between the adsorbate and the atoms of the surface are described as accurately as possible. The compromise developed here, is to use an *ab initio* method (density functional theory) to derive a potential energy surface (PES) via a series of quasi-static calculations, as a hydrogen atom is scanned across the Ni(111) surface. This PES is then used within the PACMD simulation to generate the forces on the hydrogen atom as it moves across the surface, with an explicit representation of the adsorbate and an implicit representation of the metal surface. This is valid as long as there is an adiabatic separation of the hydrogen dynamics from the nickel surface which is justified due to the large mass ratio (mass of H:Ni = 1:58.6). Hence this approach should have similar accuracy to *ab initio* dynamics but with significantly reduced computational costs.

### A. An *ab initio* potential energy surface

The density functional theory package CASTEP[17] was used to generate the PES. All calculations used a plane-wave basis set and "on the fly" ultrasoft pseudopotentials which have been shown to have excellent agreement to the "full potential" treatment[18] and the rPBE exchange-correlation functional[19]. All calculations were carried out with a 2x2 Ni (111) surface, corresponding to 0.25 ML coverage when the hydrogen atom was added, and our convergence testing on the adsorbate binding energy shows that a 2x2 supercell is sufficiently large to be equivalent to the dilute limit. The nickel surface was made up of 10 layers, as shown in figure 1, with an inter-slab spacing between neighbouring nickel surfaces of 10 Å. A cut-off energy of 725 eV, and a 4x4x1 k-point sampling grid were chosen. Full details of how these parameters were converged are in Appendix A.

The adiabatic approximation to the dynamics of the nickel-hydrogen system implies that the nickel surface remains stationary over the timescales of the faster hydrogen dynamics and that nickel ions do not have sufficient time to respond to the local position of the hydrogen at the surface. Hence we constrained the nickel ions to their minimum enthalpy configuration (in the absence of hydrogen) during the PES determination procedure. At modest temperatures (less than the Debye temperature), the nickel ions should oscillate around their equilibrium positions, and so this constraint on the nickel ions results in the average (ground state) PES neglecting any anharmonic effects.

To determine the PES, a series of constrained geometry optimisations were performed. At each point on the PES, the hydrogen was initially placed 1.5 Å above the surface and then allowed to relax to find the optimal height and energy, whilst constrained in its lateral position on the surface. Each constrained optimisation continued until the force normal to the surface was less than $2\times10^{-2}$ eV/Å, the changes in the energy per atom were less than $1\times10^{-6}$ eV per iteration, and the height change was less than $1\times10^{-4}$ Å per iteration. In practice, the requirement of such small changes in the height of the adsorbate meant that forces were actually reduced to be of the order $\sim 10^{-5}$ eV/Å. Full details of how these parameters were converged are in Appendix A.

The DFT calculations found 2 distinct minimum energy sites for the hydrogen above the surface, and 2 distinct saddle points between them. Therefore there are 4 different minimum energy transition paths as given in table I. Note that the lowest energy state corresponds to H above the second layer (sub-surface) Ni at fractional coordinates $\left(\frac{1}{3},\frac{2}{3}\right)$ which is 12 meV more stable than above the symmetry inequivalent second layer (sub-surface) Ni at fractional coordinates $\left(\frac{2}{3},\frac{1}{3}\right)$. The two barriers that will dominate the diffusion are therefore the energies to escape from the lowest minimum, which is either 130 meV or 135 meV depending on direction. As these are near-degenerate it is a reasonable approximation to analyse the data in terms of a single barrier height.

| Transition pathway | $\Delta E$ (meV) |
|---|---|
| $(\frac{1}{3}, \frac{2}{3}) \rightarrow (\frac{1}{2}, \frac{1}{2})$ | 130 |
| $(\frac{1}{3}, \frac{2}{3}) \rightarrow (\frac{1}{2}, 0)$ | 135 |
| $(\frac{2}{3}, \frac{1}{3}) \rightarrow (\frac{1}{2}, \frac{1}{2})$ | 118 |
| $(\frac{2}{3}, \frac{1}{3}) \rightarrow (\frac{1}{2}, 0)$ | 123 |

Table I: The transition energies for the lowest energy pathways of H across the Ni(111) surface, calculated using DFT. At each fractional position $(x, y)$ across the surface, H is relaxed in height.

In order to generate the effective potential $V(x, y, z)$ at any point, a Fourier interpolation procedure is used. The PES has a component $V_0(x, y; z_{opt})$ from the DFT calculations which is periodic in the $(x, y)$-plane of the Ni(111) surface, with an optimal height $z_{opt}$ at each point across the surface. To allow a full 3D dynamics without the constraint that $z = z_{opt}$ at all times, the PES is augmented with a simple quadratic potential, so:

$$V(x, y, z) = V_0(x, y; z_{opt}) + \frac{1}{2} k(x, y; z_{opt}) (z - z_{opt}(x, y))^2 \tag{1}$$

where a position-dependent spring constant $k(x, y)$ has been parameterized at the optimal height $z_{opt}$ and this optimal height is also parameterized as a function of position, i.e. $z_{opt} = z_{opt}(x, y)$. This should be valid for small oscillations of the adsorbate above the surface, beyond which anharmonic terms should be considered.

The PES is converged with three separate 16x16 grids for the relaxed DFT energies, the relaxed heights and the spring constants – see Appendix B for more details – and three 2D Fourier transforms are used to interpolate an accurate value for $V(x, y, z)$. We estimate that using the triple Fourier interpolated PES results in $\sim 6 \times 10^7$ speed up compared to the full DFT calculation – and with sub-meV accuracy. Without this speedup, it would be too computationally expensive to undertake this diffusion study.

### B. Calculation of Diffusion

At high temperatures the diffusion is expected to be thermally activated. For the simple case of a single barrier, it should follow the Arrhenius equation[20]:

$$D = D_0 \exp\left(\frac{-E_a}{k_B T}\right), \tag{2}$$

where $D$ is the diffusion coefficient, $D_0$ is the pre-factor (a constant), $E_a$ is the activation energy associated with an energy barrier, and $k_B$ is the Boltzmann constant.

At lower temperatures, there should be a cross-over to quantum diffusion, with different mechanisms including zero-point energy assisted hopping and temperature-independent quantum tunnelling. A simple estimate for this cross-over temperature can be calculated from the curvature at the top of the barrier[21] as:

$$T_c = \frac{\hbar \omega_B}{2\pi k_B} \tag{3}$$

where $\hbar$ is Planck's constant and $i\omega_B$ is the (imaginary) frequency of the particle at the top of the barrier which depends on the mass of the particle and the curvature of the barrier. Fitting a simple quadratic form to the DFT PES yields a value of $\omega_B = 8.61 \times 10^{13}$ rad/s $= 457\, cm^{-1}$ for hydrogen, and hence a cross-over temperature of $T_c \sim 105$ K for H and 74 K for D. A more sophisticated approach, e.g. the Wolynes model[22], would also include the barrier thickness and this will raise the estimate of the cross-over temperature.

Similarly, fitting a simple quadratic form to the DFT PES minimum yields $\omega_{min} = 17.4 \times 10^{13}$ rad/s $= 926\, cm^{-1}$ for hydrogen in the direction from the minimum towards the saddle point and $\omega_{min} = 15.05 \times 10^{13}$ rad/s $= 799\, cm^{-1}$ for hydrogen in the perpendicular direction. At the saddle-point, there is still a confining potential with $\omega_B =$

$20.72 \times 10^{13}$ rad/s $= 1100\, cm^{-1}$ for hydrogen in the perpendicular direction. Hence we estimate the net 2D zero-point energy contribution to reducing the effective energy barrier to be 38.7 meV for H and 27.4 meV for D.

In this work, we calculate the diffusion coefficient from molecular dynamics (MD) simulations on the *ab initio* derived PES. The MD may be classical – using the conventional MD approach of a velocity Verlet integrator[23] and a Langevin thermostat[24] to simulate the NVT ensemble – or quantum – using the partially-adiabatic centroid molecular dynamics approach (PACMD)[25] and a Langevin thermostat. Within both types of MD simulation, the diffusion coefficient may be calculated using either[23,26] a Green-Kubo or Einstein method. The Green-Kubo method uses the integral of the velocity autocorrelation function, and the Einstein method is based upon the mean squared displacement:

$$D = \frac{1}{3}\int_0^\infty \langle \mathbf{v}(0) \cdot \mathbf{v}(t) \rangle \, dt = \frac{1}{6t}\left\langle |\mathbf{r}(0) - \mathbf{r}(t)|^2 \right\rangle. \tag{4}$$

Unfortunately the decay of the velocity autocorrelation function is slow, and noise in the long-time tail of the autocorrelation function makes the accurate determination of the diffusion coefficient using this approach numerically challenging. Hence we choose to calculate the diffusion coefficient from the mean squared displacement.

### C. Diffusion and Path Integral Methods

In this section we present a brief overview of the relevant path integral molecular dynamics methods used to study diffusion.

Feynman[27] showed that there was an exact isomorphism between finite temperature quantum dynamics of a particle and the classical dynamics of a "beads and springs" system using a path integral. This provided a natural way to visualise delocalisation of the quantum particle. The mapping is exact in the limit that the number of beads $P$ per quantum particle becomes infinite. At any finite value of $P$ we have the discretised partition function for a system of $N$ quantum particles

$$Z_P = \prod_{i=1}^{N}\left(\frac{m_i P}{2\pi\beta\hbar^2}\right)^{3P/2} \int \left(\prod_{i=1}^{N}\prod_{s=1}^{P} d\mathbf{r}_{i,s}\right) \exp\left\{-\beta\left[\sum_{i=1}^{N}\frac{m_i P}{2\beta^2\hbar^2}\sum_{s=1}^{P}(\mathbf{r}_{i,s+1}-\mathbf{r}_{i,s})^2 + \frac{1}{P}\sum_{s=1}^{P} V(\mathbf{r}_{1,s},\ldots,\mathbf{r}_{N,s})\right]\right\} \tag{5}$$

where $i$ is the atom index, and $s$ is the bead index, with each particle having mass $m_i$ and being at classical position $\mathbf{r}_i$ which then becomes a "bead coordinate" $\mathbf{r}_{i,s}$ (also known as the primitive coordinate) which is periodic in $s$. Each bead interacts with the other beads of the same quantum particle through the harmonic "spring" term, and with other particles through the potential $V(\mathbf{r}_{1,s},\ldots,\mathbf{r}_{N,s})$. The temperature appears through $\beta = 1/k_B T$ as usual.

The isomorphic classical Hamiltonian therefore takes the form:

$$H = \sum_{i=1}^{N}\sum_{s=1}^{P}\left[\frac{\mathbf{p}_{i,s}^2}{2m_i'} + \frac{1}{2}m_i\omega_P^2(\mathbf{r}_{i,s+1}-\mathbf{r}_{i,s})^2\right] + \frac{1}{P}\sum_{s=1}^{P} V(\mathbf{r}_{1,s},\ldots,\mathbf{r}_{N,s}) \tag{6}$$

where the chain frequency is defined as $\omega_P = \sqrt{P}/(\beta\hbar)$, and the mass associated with the momentum variables $(\mathbf{p}_{i,s})$ is defined as $m_i' = m_i P/(2\pi\hbar)^2$. In effect, each quantum particle is replaced by a system of "beads and springs" which looks like a ring polymer. Hence MD using this isomorphic classical Hamiltonian will yield a set of configurations, and any ensemble average calculated over these configurations will be equivalent to the quantum expectation value of that operator. This is known as path integral MD, or PIMD. Straightforward PIMD using the primitive coordinates has difficulties because the harmonic nearest-neighbour interactions between beads can give ergodicity problems for simple thermostats, and a very short timestep is required to accurately integrate the equations of motion as the harmonic frequencies of the ring polymer range from $0 \to 4P/(\beta\hbar)$. These dynamics are fictitious and it is only the ensemble average that has any meaning. Hence this method, whilst a useful way to build in quantum effects such as zero-point motion, delocalisation and tunnelling, cannot be used to calculate diffusion.

The first step towards real-time quantum dynamics using path integrals came when Feynman and Kleinert[28] realised that the path centroid could be used to define a semi-classical partition function as an approximation to the true quantum partition function. This idea was then extended by Cao and Voth[16,29–32] who reformulated the imaginary time correlation function in terms of the path centroid variable and hence developed centroid molecular dynamics (CMD) as a way to calculate approximate quantum time correlation functions within a PIMD framework. In particular, they showed that the real-time correlation function is approximately:

$$C_{\text{approx}}(t) = \frac{1}{Z}\int d\mathbf{r}_c \rho_c(\mathbf{r}_c)\frac{\hbar}{2m\bar{\omega}}\left[\frac{1}{\tanh(\hbar\beta\bar{\omega}/2)}\cos(\bar{\omega}t) - i\sin(\bar{\omega}t)\right] + \langle \mathbf{r}_c\rangle^2_{\rho_c} \tag{7}$$

where $\mathbf{r}_c$ is the centroid position, $\bar{\omega}$ is some centroid-dependent effective frequency, and $\rho_c$ is the appropriate centroid density. This can be simplified with the definition of the Kubo-transformed correlation function:

$$\tilde{C}(\omega) = \frac{\hbar\beta\omega}{2}\left[1 + \coth\left(\frac{\hbar\beta\omega}{2}\right)\right]\tilde{C}^*(\omega) \tag{8}$$

where $C^*$ is known as the Kubo-transformed correlation function and $\tilde{C}$ is the Fourier transform of the original correlation function. Hence equation 7 may now be expressed as:

$$C^*_{\text{approx}}(t) = \frac{1}{Z}\int d\mathbf{r}_c \rho_c(\mathbf{r}_c)\frac{1}{m\bar{\omega}^2\beta}\cos(\bar{\omega}t) + \langle \mathbf{r}_c\rangle^2_{\rho_c} \tag{9}$$

which represents the correlation of fluctuations about the mean value. This is a short time approximation to the actual quantum correlation function. Finally, Cao and Voth generalized this by making an *ad hoc* argument that the quantum position time correlation function is related to the centroid position correlation function:

$$C^*(t) = \langle \mathbf{r}_c(t)\,\mathbf{r}_c(0)\rangle_{\rho_c(\mathbf{r}_c,p_c)} \tag{10}$$

which was physically motivated through the justification that the centroid position corresponds to the expectation value of the position along a closed path. The CMD method was later placed on a firmer mathematical footing[33,34] but the underlying ideas remain unchanged.

For a discretised path integral, the path centroid variable in terms of the primitive coordinates is simply the centre of mass of each ring polymer:

$$\mathbf{r}_c = \mathbf{r}_{i,0} = \frac{1}{P}\sum_{s=1}^{P}\mathbf{r}_{i,s}. \tag{11}$$

CMD uses the fact that the centroids evolve with a classical equation of motion using the potential of mean force generated by the beads. Conceptually, the centroid force may be calculated from a constrained-centroid PIMD trajectory using an appropriate thermostat for thermal averaging over non-centroid modes. However, this is very inefficient and computationally expensive.

A computationally more tractable approach is to enforce an adiabatic separation between the centroid mode and the bead modes, by exploiting the freedom to choose the masses associated with the momentum degrees of freedom independent of the mass associated with the harmonic bead-bead interaction. If the masses associated with the momentum degrees of freedom are made significantly lighter for the non-centroid modes than the centroid mode, then they will experience rapid oscillations around the centroid variable, when compared with the slower time evolution of the centroid itself. This means that, by choosing these masses in a suitable way, and strongly thermostatting the non-centroid modes, the phase space sampling of the non-centroid modes should be ergodic on the timescales of the slower centroid mode, and the centroid force (the potential of mean force generated by the non-centroid modes) will be generated correctly "on the fly" — without any explicit constraints on the centroid position.

To do this efficiently, we use the normal mode transformation[26], which makes the frequency of all modes equal to $\sqrt{P}/\hbar\beta$[25]. Without a transformation like this, the ring polymer has a wide range of normal mode frequencies (which increase with $P$) and hence requires a smaller MD timestep. The normal mode transformation also leads to a natural identification of the centroid mode, which is the zero frequency normal mode of the ring polymer, and makes enforcing the adiabatic separation trivial.

The transformation from the primitive variables to the normal mode variables[26] is an orthogonal matrix ($O$) which can be constructed by diagonalization of the monodromy matrix ($A$), which is defined as:

$$A_{ij} = 2\delta_{ij} - \delta_{i,j-1} - \delta_{i,j+1}, \quad ; \quad i,j = 1,...,P \tag{12}$$

which has path periodicity: i.e. for $j-1$ and $j+1$, $0 \to P$ and $P+1 \to 1$, as expected from the periodicity of the ring polymer.

After constructing and diagonalising the monodromy matrix, the eigenvalues, $\lambda$, are:

$$\lambda_{2k-1} = \lambda_{2k-2} = 2\left[1 - \cos\left(\frac{2\pi\,(k-1)}{P}\right)\right] \tag{13}$$

where $k$ is the mode index.

The forward transformation from primitive mode variables, $\mathbf{r}_{i,s}$ to normal mode variables, $\mathbf{u}_{i,k}$ is:

$$\mathbf{u}_{i,k} = \frac{1}{\sqrt{P}} \sum_{s=1}^{P} O_{ks}^{T} \mathbf{r}_{i,s}, \tag{14}$$

and so the position of the centroid becomes equal to $\mathbf{u}_{i,1}$, which is

$$\mathbf{u}_{i,1} = \frac{1}{P} \sum_{s=1}^{P} \mathbf{r}_{i,s}. \tag{15}$$

In order to evolve the normal mode coordinates, we also require the forces acting on them. These can be calculated from the knowledge of the forces (which are calculated using the PES) acting on the primitive variables:

$$\frac{1}{P}\frac{\partial V}{\partial \mathbf{u}_{i,1}} = \frac{1}{P} \sum_{s=1}^{P} \frac{\partial V}{\partial \mathbf{r}_{i,s}} \tag{16}$$

$$\frac{1}{P}\frac{\partial V}{\partial \mathbf{u}_{i,k}} = \frac{1}{\sqrt{P}} \sum_{s=1}^{P} \frac{\partial V}{\partial \mathbf{r}_{i,s}} O_{sk}. \tag{17}$$

To enforce the adiabatic separation we rescale the masses associated with the momentum degrees of freedom ($m'$) of the non-centroid modes leading to the introduction of an additional parameter, $\gamma$, known as the *adiabaticity parameter*[25,35] whereupon these masses now depend upon the bead index as: $m'_{i,k} = \gamma^2 m_i \lambda_k$, $m'_{i,1} = m_i$, and $m'_{i,k} = m_{i,k}$. The isomorphic Hamiltonian may then be written in terms of the normal modes as

$$H = \sum_{i=1}^{N} \sum_{k=1}^{P} \left[ \frac{p_{i,k}^2}{2m'_{i,k}} + \frac{1}{2} m_{i,k} \omega_P^2 u_{i,k}^2 + \frac{1}{P} V\left(\mathbf{u}_{i,k}\right) \right]. \tag{18}$$

Early CMD papers advocated a complete adiabatic separation between the centroid and non-centroid modes, but as the amount of adiabaticity increases, i.e. as $\gamma \to 0$, the normal mode frequencies oscillate more quickly, and we require a smaller timestep to accurately integrate the equations of motion. It was later shown by Hone *et al*[25] that a partial adiabatic separation can lead to accurate time correlation functions but with large gains in computational efficiency due to using a larger timestep. In effect, $\gamma$ becomes another convergence parameter (along with $P$) of the method, which is therefore known as Partially-Adiabatic Centroid Molecular Dynamics (PACMD). This is the method that we used to study the diffusion of hydrogen.

A conceptually similar approach, Ring Polymer Molecular Dynamics (RPMD), was independently developed by Manolopoulos *et al* [36,37] and can also be used to calculate real-time correlation functions.

## III. RESULTS

### A. Diffusion studied with classical MD

Initial studies using classical NVT-ensemble MD (with a Langevin thermostat) and the *ab initio* PES showed that converged diffusion coefficients could be calculated using a Langevin damping time of 500 fs, a time step of 1 fs, total simulation time of 10 ns, discarding first 0.5 ns of each trajectory and averaging over at least 20 independent

trajectories. Time-origin averaging within each trajectory was also used to improve the statistics of the diffusion coefficient calculation. All MD calculations were performed using the authors' own code[38]. Full details are in Appendix C.

It is observed that classically the diffusion rate varies by 6 orders of magnitude over the temperature range 100 K to 250 K as shown in the Arrhenius plot in figure 2 although there is increasing uncertainty at low temperatures due to the 'rare event' nature of the classical process.

The activation energies and pre-factors associated with the adsorbate diffusion were then calculated by fitting the Arrhenius relationship, leading to the results given in table II.

| | $D_0$ $(cm^2/s)$ | $E_a$ (meV) |
|---|---|---|
| H | $6.29 \times 10^{-4}$ | 118.5 |
| D | $5.06 \times 10^{-4}$ | 120.1 |

Table II: Pre-factors and activation energies from the Arrhenius law, for classical H and D on the Ni(111) surface.

As classical diffusion occurs via thermally activated hopping over free energy barriers, it is the barrier height which determines the activation energy, rather than the shape of the energy barrier (as in quantum tunnelling). This means that, because the PES is identical for H and D, that the activation energies should be the same for classical diffusion. Instead, we find a slight (1.6 meV) difference which may be attributed to the 'rare event' nature of diffusion at low temperatures and suggests the likely accuracy of the barrier height calculation. Note that the H:D ratio between the pre-factors is found to be 1.2, which is only slightly smaller than the expected $\sqrt{m_D/m_H} \simeq 1.4$. Note also that the barrier height is slightly smaller than the 130 meV barrier found in the (T=0) DFT calculations, which is to be expected as this is a free energy barrier.

Further insight into the mechanism of diffusion can be gained by visualisation of the trajectories. Figure 3 shows the motion of H and D across the PES at a temperature of 250 K for 500 ps. The adsorbate appears to spend a large amount of time in the two minima of the PES (because of the large number of data points in these regions), before thermally hopping to another of the minima, via the bridge site — this gives rise to a trajectory which appears to have a characteristic hexagonal pattern, which arises out of the structure of the (111)-surface of (FCC) nickel. The sites above the surface atoms are energetically unfavourable, and are not explored by the adsorbate during this comparatively short MD trajectory.

### B. Diffusion studied with PACMD

The optimal adiabaticity parameter value for the PACMD simulations was found to be $\gamma = 0.01$, which necessitated a smaller timestep than for non-centroid PIMD or classical MD, and the largest stable timestep was 0.05 fs. The quantum properties were fully converged when using 16 beads per quantum particle. Further details on how these values were chosen are in Appendix C. As with the classical calculations, the diffusion rate was calculated from the mean squared displacement, for both H and D on the Ni(111) surface (as approximated by the *ab initio* PES) at temperatures ranging from 75 K to 250 K, with a Langevin damping time of 500 fs. For each of these calculations, we ran for a total simulation time of 2.5 ns, with a timestep of 0.05 fs. This time, at each value of the temperature (for each isotope), a set of 12 independent trajectories was computed, in order to allow for an averaging over several diffusion coefficients to improve the quality of the final diffusion coefficients, as well as allowing an estimate of the error. The statistics for each diffusion coefficient were further improved by calculating the correlation function over a time period of 0.95 ns, allowing for time origin averaging for each trajectory. The diffusion coefficient, particularly at low temperatures, is dramatically enhanced, and now only varies by 2 orders of magnitude (not 6 as in classical MD) over the temperature range considered. Hence the temperature range was extended below the classical MD limit (100 K) down to 75 K where there was still a significant amount of diffusion. As with the classical simulations, all PACMD calculations were performed using the authors' own code[38].

The PACMD calculated diffusion coefficients are shown as an Arrhenius plot in figure 4 which shows a dramatic increase over that seen in classical simulations (figure 2). A single straight-line fit is no longer appropriate and there is clear evidence of a break in the Arrhenius slope at low temperatures. By considering all possible 2-line fits, the statistically optimal break was found to be around 150 K for hydrogen and 85 K for deuterium. This break suggests a transition from thermally activated (classical) tunnelling at high temperatures, and the more temperature independent diffusion through quantum tunnelling at lower temperatures. The transition is not as sharp as expected from a simple model, suggesting that there are multiple competing processes – for instance, the zero-point energy will raise the energy of the absorbate and therefore require less thermal energy to activate over a barrier, which is

therefore a mixed quantum/classical process that is still important near the transition. A Fisher F-test shows that the 2-line fit is statistically justified (5% level) for both hydrogen and deuterium, but a 3-line fit is not justified.

The activation energies and pre-factors associated with the adsorbate diffusion were then calculated by fitting the Arrhenius relationship to both lines, leading to the results given in table III. We now find that the activation barrier is significantly reduced from the 120 meV barrier found in the classical simulations, which shows that quantum effects, such as zero-point energy (estimated above from the DFT PES as being 38.7 meV for H and 27.4 meV for D), make a very significant contribution to the dynamics at all temperatures. In addition, the ratio of the pre-factors is now found to be 1.55 in the high temperature regime (as for the classical simulations) but 2.95 in the low temperature region, i.e. significantly enhanced. These results are a further indication that the diffusion mechanism is significantly different as temperature is decreased in the PACMD simulation compared with classical MD. The difference betwen H and D activation energies at high temperature is slightly larger (4.2 meV) than the classical calculations (1.6 meV) which is a guide to reliability of the fitting procedure and the different size of the data sets. The low temperature difference is remarkably small at only 0.2 meV, which suggests a robustness in the quantum dynamics.

| | $D_0$ $(cm^2/s)$ | $E_a$ (meV) |
|---|---|---|
| H (250 - 150 K) | $7.41 \times 10^{-4}$ | 44.4 |
| H (150 - 75 K) | $1.36 \times 10^{-4}$ | 23.1 |
| D (250 - 85 K) | $4.78 \times 10^{-4}$ | 40.2 |
| D (85 - 75 K) | $0.46 \times 10^{-4}$ | 22.9 |

Table III: Pre-factors and activation energies (given to 3 significant figures) from the Arrhenius law, for quantum H and D (16 beads) on the Ni(111) surface. These values are calculated separately for the (isotope dependent) high and low temperature regions.

In the classical MD simulation, the only difference between H and D diffusion arose from the mass difference, and there was no qualitative difference between the diffusion of H and D, which is not the case in the quantum regime. The H:D ratio of the diffusion coefficients in both classical MD and PACMD simulation can be seen in figure 5. Whilst the ratio of the two diffusion coefficients is similar both classically and quantum mechanically at higher temperatures (150 K to 250 K), there appears to be a widening between the ratios of the classical and quantum results as the temperature reduces.

The ratio of the two diffusion coefficients in the classical MD should remain more or less constant across the whole temperature range as there is only a single mechanism by which diffusion can occur. In the quantum results, as the temperature decreases, there are multiple mechanisms by which the adsorbate can diffuse across the surface and so it is expected that there should be some change in the ratios as the temperature decreases. The expected behaviour was observed: that the hydrogen diffusion rate will increase more rapidly than the deuterium rate, owing to its larger amount of delocalisation and zero-point energy.

Further insight can be gained by visualisation of the trajectories. We plot the centroid position from the PACMD simulation and superimpose a circle representing the radius of gyration at each timestep, illustrating which regions the quantum adsorbate "feels" as it diffuses across the surface. Figure 6 shows the motion of H and D across the PES at a temperature of 250 K for 200 ps. The adsorbate appears to spend a large amount of time in the two minima of the PES (as indicated by the large number of data points in these regions), before thermally hopping to another of the minima via the bridge site — this gives rise to a trajectory which appears to have the same characteristic hexagonal pattern. As expected, hydrogen is more mobile and more delocalised than deuterium, and so has a greater mean displacement and a larger radius of gyration.

Due to the large distances shown in figure 6, it is difficult to see the extent of the delocalisation of the adsorbate on this scale. In order to show the extent of the delocalisation as a function of adsorbate position across the surface, figure 7 shows an enlarged region of a subset of the two trajectories. Note that because these two trajectories took different pathways, the absolute positions shown are different for both particles, but due to the periodicity of the underlying potential energy surface, the adsorbate would be subject to the same potential energy derived forces in these regions. The sites above the surface atoms are energetically unfavourable, and in the classical MD simulations (figure 3) are not explored by the adsorbate during this comparatively short MD trajectory. However, in the enlarged section shown in figure 7 it can be seen that there are now some regions where the adsorbate deviates slightly from this path e.g. by passing over a site above one of the topmost nickel surface atoms. This is not unexpected as the Langevin thermostat should excite the adsorbate over any barrier at some point, with the quantum delocalisation increasing the likelihood of such motion.

Figure 8 shows the quantum trajectories of H and D across the PES at a temperature of 75 K for 200 ps. Note that even though the visualised trajectory is shorter than the corresponding classical trajectories (250 K for 500 ps)

in figure 3, the adsorbates are shown to explore a similar amount of the PES. We still see the same characteristic hexagonal structure emerging, but enhanced "smearing" due to the delocalised nature of the adsorbates.

We see the hydrogen is not only more mobile than the deuterium, but it is also more delocalised as well. There is also an indication that the adsorbate becomes more delocalised in the minima of the potential than across the bridge site which is to be expected, as the PES curvature is smaller at the minima than across the bridge site (due to the position of the topmost nickel atoms). In these calculations, although there does not appear to be any indication of the ring polymer extending directly over the sites above the topmost nickel atoms, there is a significant amount of delocalisation extending into this region, where the classical particle would be unlikely to explore.

## IV. DISCUSSION

At all temperatures studied, the PACMD simulations resulted in significantly larger diffusion coefficients than the classical results, as shown in figure 9. It is observed that the quantum diffusion rates span many fewer orders of magnitude than the classical results, and also that there is strong evidence of a quantum transition in the diffusion mechanism at around 150 K in hydrogen and 85 K in deuterium. This shows that, not only are the classical results quantitatively wrong, but that they also show qualitative differences when compared with the quantum simulations, especially at low temperatures.

Compared to the experimental results which motivated this work, we find that all our PACMD diffusion rates are consistently faster than diffusion rates reported Lin *et al*[6], Lee *et al*[7] and Cao *et al*[8]. However, compared to the newer (preliminary) experimental results of Ward *et al*[13] (whose results suggest diffusion rates of $\sim 10^{-6}$ to $10^{-7}$ cm$^2$/s across a temperature range of 250 K to 125 K, and a transition temperature of approximately 170 K), we find that our classical diffusion rates are very similar at 250 K, but differ by around an order of magnitude as the temperature decreases to 150 K. At low temperatures, our classical simulations have a much lower diffusion coefficient than seen by Ward *et al*[13]. This is encouraging, because we should naturally expect that the system behaves classically at higher temperatures, but should report slower diffusion rates than the physical system as the temperature decreases due to the neglect of quantum effects in the classical MD calculations, whereas the PACMD simulations have a markedly increased diffusion rate across the whole temperature range. Compared to the results of Ward[13] our diffusion coefficients are typically larger than the experimental results by 2 orders of magnitude, and in addition we find a less sharply defined transition temperature, at around 150 K. However, the PACMD diffusion coefficients now span the same number of orders of magnitude as the experimental results of Lin[6], Cao[7] and Ward[13] (even though the absolute rates are different). The PACMD transition from classical to quantum diffusion is not as sharp as seen in the experiments, except those of Cao[8] (who report a much more gradual change in the gradient of the Arrhenius plot — with a transition temperature of 110 K). We also note that almost all of the experimental results show a continuous change in the gradient of the Arrhenius plot, before finally transitioning to relatively temperature independent diffusion (with the exception of Cao[8], whose diffusion coefficients still vary significantly beyond this transition), whereas our quantum results still vary (by a small amount) below the cross-over temperature.

The quantum diffusion of H or D on Ni(111) surface has been calculated using PACMD of a single quantum particle with an *ab initio* derived PES. This PES represents the interaction of H with Ni(111) and has been converged carefully to the given level of *ab initio* theory. The PACMD calculations have also been carefully converged with the given PES. The use of an *ab initio* derived PES in this way is expected to yield more reliable and predictive results than those based upon a semi-empirical treatment. Hence the only significant remaining approximation is the use of a fixed PES which means that the Ni(111) surface is treated as static. It was earlier argued that this effect would be small due to the large mass ratio (mass of H:Ni = 1:58.6), and indeed, an RPMD-based study of H diffusion on the related Ni(100) surface[39] using a semiempirical treatment for the H-Ni interactions showed that the effect of Ni dynamics on the H diffusion was generally small, and indeed, our results with a static surface are in good general agreement with the different experimental results. A dynamic surface would, however, have a larger affect on deuterium diffusion which might explain the anomalous isotope scaling seen in the results of Ward *et al*[13].

## V. CONCLUSIONS

We have used DFT to calculate the static interaction of H with the Ni(111) surface, and then used this to create a potential energy surface. This potential energy surface is then used to dramatically speed up the diffusion simulations, using either classical MD or quantum PACMD. Studies using classical MD yield diffusion coefficients that are much too small compared to experiment, especially at low temperature, and vary by too many orders of magnitude across the temperature range studied (250 K to 100 K). The use of PACMD makes a dramatic difference to the mechanism of diffusion, and increases the absolute values of the diffusion coefficient, and reduces the temperature variation markedly.

The PACMD simulations (250 K to 75 K) also demonstrate a cross-over to quantum-dominated diffusion below 150 K for H and 85 K for D.

Hence we have demonstrated using PACMD that quantum nuclear effects are essential in the treatment of the diffusion of H and D across the Ni(111) surface at all temperatures studied.

## VI. ACKNOWLEDGMENTS

We are grateful for computational support from the UK national high performance computing service, ARCHER, for which access was obtained via the UKCP consortium and funded by EPSRC grant ref EP/P022561/1. Additional calculations made use of the facilities of the N8 HPC Centre of Excellence, provided and funded by the N8 consortium and EPSRC grant ref EP/K000225/1). We acknowledge useful discussions with Jolyon Aarons, Phil Hasnip and Ed Higgins.

---

* Present address: Met Office, FitzRoy Road, Exeter, Devon, EX1 3PB, United Kingdom
† Author to whom correspondence should be addressed

[1] T. Graham, Phil. Trans. R. Soc. Lond. **156**, 399 (1866).
[2] H. Wipf, *Diffusion of hydrogen in metals* (Springer Berlin Heidelberg, 1997).
[3] W. H. Johnson, Proc. R. Soc. Lond. **23**, 168 (1875).
[4] Y. Chung, Tech. Rep., Toll bridge program oversight committee (2014).
[5] H. K. D. H. Bhadeshia, ISIJ International **56**, 24 (2016).
[6] T. S. Lin and R. Gomer, Surf. Sci. **255**, 41 (1991).
[7] A. Lee, X. D. Zhu, A. Wong, D. L., and U. Linke, Phys. Rev. B **48**, 11256 (1993).
[8] G. X. Cao, E. Nabighian, and X. D. Zhu, Phys. Rev. Lett. **79**, 3696 (1997).
[9] A. P. Jardine, H. Hedgeland, G. Alexandrowicz, W. Allison, and J. Ellis, Prog. Surf. Sci. **84**, 323 (2009).
[10] A. P. Jardine, G. Alexandrowicz, H. Hedgeland, W. Allison, and J. Ellis, Phys. Chem. Chem. Phys. **11**, 3355 (2009).
[11] A. P. Jardine, E. Y. M. Lee, D. J. Ward, G. Alexandrowicz, H. Hedgeland, W. Allison, J. Ellis, and E. Pollak, Phys. Rev. Lett. **105**, 136101 (2010).
[12] E. M. McIntosh, K. T. Wilkfeld, J. Ellis, A. Michaelides, and W. Allison, J. Phys. Chem. Lett. **4**, 1565 (2013).
[13] J. Zhu and D. Ward (2013), private communication.
[14] B. J. Berne and D. Thirumalai, Ann. Rev. Phys. Chem. **37**, 401 (1986).
[15] M. E. Tuckerman, B. J. Berne, G. J. Martyna, and M. L. Klein, J. Chem. Phys. **99**, 2796 (1993).
[16] J. Cao and G. A. Voth, J. Chem. Phys. **99**, 10070 (1993).
[17] S. J. Clark, M. D. Segall, C. J. Pickard, P. J. Hasnip, M. J. Probert, K. Refson, and M. Payne, Z. Kristall. **220**, 567 (2005).
[18] K. Lejaeghere, G. Bihlmayer, T. Björkman, P. Blaha, S. Blügel, V. Blum, D. Caliste, I. E. Castelli, S. J. Clark, A. D. Corso, et al., Science **351**, aad3000 (2016).
[19] B. Hammer, L. B. Hansen, and J. K. Nørskov, Phys. Rev. B **59**, 7413 (1999).
[20] P. Atkins and J. de Paula, *Atkins' Physical Chemistry* (Oxford University Press, 2006), 8th ed.
[21] M. J. Gillan, J. Phys. C **20**, 3621 (1987).
[22] P. G. Wolynes, Physical Review Letters **47**, 968 (1981).
[23] M. P. Allen and D. J. Tildesley, *Computer Simulation of Liquids* (Clarendon Press, Oxford, 1987).
[24] S. Chandrasekhar, Rev. Mod. Phys. **15**, 1 (1943).
[25] T. D. Hone, P. J. Rossky, and G. A. Voth, J. Chem. Phys. **124**, 154103 (2006).
[26] M. E. Tuckerman, *Statistical Mechanics: Theory and Molecular Simulation* (Oxford Graduate Texts, Oxford University Press, 2010).
[27] R. P. Feynman, A. R. Hibbs, and D. F. Styer, *Quantum Mechanics and Path Integrals* (Dover Publications, 2010), emended ed.
[28] R. P. Feynman and H. Kleinert, Phys. Rev. A **34**, 5080 (1986).
[29] J. Cao and G. A. Voth, J. Chem. Phys. **100**, 5093 (1994).
[30] J. Cao and G. A. Voth, J. Chem. Phys. **100**, 5106 (1994).
[31] J. Cao and G. A. Voth, J. Chem. Phys. **101**, 6157 (1994).
[32] J. Cao and G. A. Voth, J. Chem. Phys. **101**, 6168 (1994).
[33] S. Jang and G. A. Voth, J. Chem. Phys. **111**, 2357 (1999).
[34] S. Jang and G. A. Voth, J. Chem. Phys. **111**, 2371 (1999).
[35] J. Cao and G. J. Martyna, J. Chem. Phys. **104**, 2028 (1996).
[36] I. R. Craig and D. E. Manolopoulos, Journal of Chemical Physics **121**, 3368 (2004).
[37] S. Habershon, D. E. Manolopoulos, T. E. Markland, and T. F. Miller III, Ann. Rev. Phys. Chem. **64**, 387 (2013).
[38] A. R. Hopkinson, *Spring version 1*, URL `DOI:10.5281/zenodo.852632`.
[39] Y. V. Suleimanov, J. Phys. Chem. C **116**, 11141 (2012).

[40] C. Kittel, *Introduction to Solid State Physics* (John Wiley & Sons, 2005), 8th ed.
[41] P. Langevin, C. R. Acad. Sci. (Paris) **146**, 530 (1908).
[42] D. S. Lemons and A. Gythiel, Am. J. Phys. **65**, 1079 (1997).
[43] J. E. Lennard-Jones, Proc. R. Soc. London, Ser. A. **106**, 463 (1924).
[44] J. E. Lennard-Jones, Proc. Phys. Soc. **43**, 461 (1931).
[45] G. Bussi and M. Parrinello, Comp. Phys. Comm. **127**, 26 (2008).

## Appendix A: Convergence of the DFT calculation

All the DFT calculations presented here used the periodic plane-wave code CASTEP[17] and so the two primary convergence parameters which affect all results are the basis set size (plane wave cut-off energy) and sampling of the Brillouin zone (**k**-point sampling density). To study a surface with periodic boundary conditions, we also need to converge the inter-slab spacing (vacuum gap size), the number of layers that make up the nickel surface, and the concentration of hydrogen on the surface (to determine the dilute limit). The DFT calculations are ultimately used to calculate a potential energy surface across which the hydrogen dynamics can take place. For this reason, the quantity of interest that is computed during convergence testing is the binding energy:

$$E_{\text{bind}} = E\left(\text{Ni} + \text{H}\right) - \left[E\left(\text{Ni}\right) + E\left(\text{H}\right)\right]. \tag{A1}$$

When calculating the binding energy, $E\left(\text{Ni} + \text{H}\right)$ is the total energy of the nickel system (bulk or surface, depending on the calculation) with a hydrogen atom placed 1.5 Å above the topmost nickel layer, $E\left(\text{Ni}\right)$ is the total energy of the same system but without the hydrogen, and $E\left(\text{H}\right)$ is total energy of the same size simulation cell containing only the hydrogen atom. All the DFT calculations are spin polarised, to allow for possible magnetic states to spontaneously arise.

### 1. Basic DFT convergence of the bulk system

In order to determine convergence, the binding energy for a hydrogen atom placed in a bulk nickel system was calculated as a function of the plane-wave cut-off energy. These calculations were carried out using a relatively coarse 3x3x3 **k**-point grid and in all cases, the geometry of the structure was kept constant. It was found that the change in the binding energy reduces to 0.6 meV at a cut-off energy of 725 eV (relative to a cut-off energy of 750 eV).

Unlike the convergence of the cut-off energy, the convergence of binding energy with respect to **k**-point density is not smoothly varying, and exhibits oscillations as the dimensions of the **k**-point grid are increased. The convergence behaviour of the binding energy with respect to Brillouin zone sampling (fixed cut-off energy of 400 eV) for the same bulk system as was used for the cut-off energy convergence is presented in figure 10.

With the cut-off energy and **k**-point grid dimensions determined (725 eV and 7x7x7 grid, respectively), a variable cell geometry optimisation was then performed on the bulk nickel system to determine the lattice constant. The lattice constant was found to be 3.5549 Å. For this lattice constant, the maximum component of the stress tensor was reduced to $3.43 \times 10^{-6}$ GPa. (By symmetry, the force on each of the nickel ions was zero).

### 2. Convergence of surface calculations

The previously optimised bulk structure was used as the basis for all surface calculations using the supercell technique. The bulk cell was composed of 3 atoms (forming 3 layers), and was oriented such that, as a vacuum gap is introduced above the topmost layer, the (111) surface is exposed (ensuring the same **k**-point sampling in the surface plane as the subsequent surface calculations). As the vacuum gap is increased, the separation between periodic images is increased, and so the Brillouin zone sampling only requires a single grid point in that direction.

The change in binding energy for a hydrogen atom placed 1.5 Å above a 4 layer thick (111) nickel surface, as a function of vacuum gap size/inter-slab spacing is presented in figure 11 (725 eV cut-off energy and 7x7x1 **k**-point grid). In all cases, the interlayer spacing of the nickel surface is kept constant (we do not perform geometry optimisations as the size of the vacuum gap is varied).

The convergence of the binding energy with respect to the number of layers forming the surface is given in figure 12. These calculations were again performed by placing a hydrogen atom 1.5 Å above the topmost layer of the surface, with an inter-slab spacing fixed at 6 Å, a 725 eV cut-off energy, and a 7x7x1 **k**-point grid. In these calculations, the ABCA stacking that is characteristic of the (111) surface of an FCC material (with no centre of inversion symmetry)[40] was always preserved. Again, the interlayer spacing of the nickel surface was kept constant as the number of layers were increased.

Finally, the effect of the hydrogen concentration was evaluated by studying different sized supercells of the Ni(111) surface in the **a** and **b** directions, whilst keeping the number of hydrogen ions fixed. All calculations are carried out with a 10 Å inter-slab spacing, 10 layers of nickel forming the (111) surface (preserving ABCA stacking), and a 725 eV cut-off energy.

In order to ensure a fair comparison between the true binding energies, constrained variable cell geometry optimisations were first carried out on the nickel-only systems. The constraints acted to fix the position of the middle layer of the nickel surface, and ensured that the cell vector (normal to the surface) did not compress to a more bulk-like state. This process ensured that the effect of the different **k**-point sampling densities were always fully accounted for, with the surface lattice constants, and interlayer spacing of the nickel slab able to vary. In all instances, the geometry optimisations were performed until the maximum force was reduced to less than $2.5 \times 10^{-2}$ eV/Å and the maximum component of the stress tensor was less than $1 \times 10^{-2}$ GPa.

With the optimal geometry of the nickel surfaces determined, a single hydrogen atom was then placed 1.5 Å above the surface (above the same site of each supercell surface, such that the binding energies were comparable), and a further geometry optimisation was performed with all cell vectors fixed, and the hydrogen atom constrained to move only along a direction normal to the surface. For this geometry optimisation, the hydrogen height above the surface was varied until the force on the atom was reduced to $2.5 \times 10^{-2}$ eV/Å.

Table IV shows the binding energies as a function of the hydrogen concentration on the surface. For equivalent **k**-point sampling densities, we see that the change in binding energy between the 1.0 ML (1x1) coverage system and the 0.25 ML (2x2) coverage is 25.7 meV, but the difference between the 0.25 ML (2x2) coverage and the 0.0625 ML (4x4) coverage is 0.2 meV. Therefore the 0.25 ML coverage system can be considered to be a suitable approximation to the dilute limit.

| Supercell size (**k**-point sampling) | Binding energy (eV) | $\Delta E_{\text{bind}}$ (meV) (compared with supercell size) |
|---|---|---|
| 1x1 (k: 8x8x1) | -2.1681 | -25.7 (2x2) |
| 1x1 (k: 9x9x1) | -2.1839 | -17.7 (3x3) |
| 1x1 (k:10x10x1) | -2.1652 | -20.0 (5x5) |
| 2x2 (k: 4x4x1) | -2.1424 | -0.2 (4x4) |
| 3x3 (k: 3x3x1) | -2.1662 | - |
| 4x4 (k: 2x2x1) | -2.1422 | - |
| 5x5 (k: 2x2x1) | -2.1452 | - |

Table IV: Binding energies for a hydrogen atom placed above a 10 layer thick (111) nickel surface (with a 10 Å inter-slab spacing), as a function of the supercell size (concentration of hydrogen).

### 3. Summary of DFT calculation parameters

When determining the potential energy surface using CASTEP, a cut-off energy of 725 eV was chosen to reduce the difference in binding energy to 0.6 meV (compared with a 750 eV cut-off), and a Monkhorst-Pack **k**-point sampling grid of dimensions 4x4x1 on a 2x2 supercell of the nickel surface was also chosen. This **k**-point grid corresponds to an 8x8x1 grid on the 1x1 surface supercell, which has a difference in binding energy of 2.9 meV when compared with the 10x10x1 sampling on the same size supercell. The nickel surface was composed of 10 layers (resulting in a binding energy difference of 1.8 meV between 10 and 13 layers). The inter-slab spacing was chosen to be 10 Å (giving a change in binding energy of 0.04 meV when compared with a 15 Å spacing). It was shown that a concentration of 0.25 ML coverage of hydrogen turns out to be a reasonable approximation to the dilute limit. This concentration corresponds to a single hydrogen atom for every 2x2 supercell of the nickel surface. The difference in binding energy between a hydrogen atom placed on a 2x2 surface and a one placed at an equivalent site on a 4x4 surface (with equivalent **k**-point sampling) was found to be 0.2 meV.

## Appendix B: Convergence of the PES

The determination of the PES is a computationally demanding procedure, and the number of data points used to fit the PES must be increased until convergence is reached. With the functional form given in equation 1, each of the three grids (minimum energies, spring constants and equilibrium heights) that are Fourier interpolated, may be of arbitrary size. In order to determine at which point convergence is reached, the interpolated data is compared against a validation set of 16 data points. The points which make up the validation set were hydrogen positions that were randomly generated across the surface and then relaxed vertically, and these data were not used in any of the fitting procedures.

### 1. Interpolation of relaxed energies

The statistics showing the quality of the interpolation (when compared to the validation set) as a function of the size of the interpolation grid is given in table V.

| Grid Size | $\overline{\Delta E}$ (meV) | $\Delta E_{\min}$ (meV) | $\Delta E_{\max}$ (meV) |
|---|---|---|---|
| 1x1 | -254 | -5.96 | -488 |
| 2x2 | 87.3 | -1.03 | 3.14 |
| 4x4 | 3.14 | -1.23 | -77.9 |
| 8x8 | -1.05 | 0.0213 | -4.19 |
| 16x16 | -0.309 | 0.0194 | -1.84 |

Table V: The statistics of the energy difference between the interpolated values and the validation set, calculated using DFT. The mean energy difference $\overline{\Delta E}$ reduces to meV level for the 8x8 grid, and is reduced to the sub-meV level for the 16x16 grid.

This shows that the (relative) energy is converged with a 16x16 grid and this interpolated surface is presented in figure 13.

It is very interesting to note that the energy surface has 2 distinct minima and 2 distinct saddle points and therefore 4 different minimum energy transition paths as given in table VI.Note that the lowest energy state corresponds to H above the second layer (sub-surface) Ni at fractional coordinates $\left(\frac{1}{3}, \frac{2}{3}\right)$ which is 12 meV more stable than above the symmetry inequivalent second layer (sub-surface) Ni at fractional coordinates $\left(\frac{2}{3}, \frac{1}{3}\right)$. The two barriers that will dominate the diffusion are therefore the energies to escape from the lowest minimum, which 130 meV and 135 meV depending on direction. As these are near-degenerate it is a reasonable approximation to analyse the data in terms of a single barrier height.

| Transition pathway | $\Delta E$ (meV) |
|---|---|
| $\left(\frac{1}{3}, \frac{2}{3}\right) \rightarrow \left(\frac{1}{2}, \frac{1}{2}\right)$ | 130 |
| $\left(\frac{2}{3}, \frac{1}{3}\right) \rightarrow \left(\frac{1}{2}, \frac{1}{2}\right)$ | 118 |
| $\left(\frac{1}{3}, \frac{2}{3}\right) \rightarrow \left(\frac{1}{2}, 0\right)$ | 135 |
| $\left(\frac{2}{3}, \frac{1}{3}\right) \rightarrow \left(\frac{1}{2}, 0\right)$ | 123 |

Table VI: The transition energies for the lowest energy pathways of H across the Ni(111) surface, calculated using DFT. At each fractional position $(x, y)$ across the surface, H is relaxed in height.

### 2. Interpolation of relaxed heights

The statistics showing the quality of the interpolation (when compared to the validation set) as a function of the size of the interpolation grid is given in table VII. As would be expected, there is a direct relationship between the potential energy and the binding height, which arises due to the atomic structure of the surface (with lowest energy sites above the hollow sites of the surface).

| Grid Size | $\overline{\Delta z_0}$ (mÅ) | $\Delta z_{0\min}$ (mÅ) | $\Delta z_{0\max}$ (mÅ) |
|---|---|---|---|
| 1x1 | -280 | -4.84 | -511 |
| 2x2 | 78.6 | 0.326 | 302 |
| 4x4 | 4.06 | 0.190 | -66.7 |
| 8x8 | 0.185 | 0.0234 | 4.30 |
| 16x16 | 0.107 | 0.00737 | 0.691 |

Table VII: The statistics of the difference in equilibrium hydrogen height between the interpolated values and the validation set, calculated using DFT. The mean height difference $\overline{\Delta z_0}$ reduces to sub-mÅ level for the 8x8 grid.

This shows that the (relative) height is converged with a 16x16 grid and this interpolated surface is presented in figure 14.

### 3. Interpolation of spring constants

In order to calculate the sping constant at each $(x, y)$ position across the surface, we performed a least-squares fit to $\sqrt{|E - E_0|} = \frac{1}{2}k\,|z - z_0|$ using the previously determined optimal $E_0$ and $z_0$. The statistics showing the quality of the interpolation (when compared to the validation set) as a function of the size of the interpolation grid is given in table VIII.

| Grid Size | $\overline{\Delta k}$ (eV/Å$^2$) | $\Delta k_{\min}$ (eV/Å$^2$) | $\Delta k_{\max}$ (eV/Å$^2$) |
|---|---|---|---|
| 1x1 | $-6.36$ | $-1.20 \times 10^{-1}$ | $-9.20$ |
| 2x2 | $3.39 \times 10^{-1}$ | $-2.33 \times 10^{-2}$ | 3.68 |
| 4x4 | $-4.33 \times 10^{-1}$ | $-5.19 \times 10^{-2}$ | $-1.15$ |
| 8x8 | $-1.60 \times 10^{-1}$ | $3.00 \times 10^{-2}$ | $-6.74 \times 10^{-1}$ |
| 16x16 | $4.64 \times 10^{-3}$ | $-7.95 \times 10^{-3}$ | $4.55 \times 10^{-1}$ |

Table VIII: The statistics of the difference in spring constant between the interpolated values and the validation set, calculated using DFT. The mean difference in spring constant $\overline{\Delta k}$ drops by two orders of magnitude as the grid dimensions increase from 8x8 to 16x16. There is also a very large spread in values for grid sizes smaller than the 8x8.

The interpolated spring constant surface is less smooth than the corresponding energy and height surfaces, especially in the regions above the low energy sites (corresponding to the hollow sites of the surface). However, the variation in the spring constant is not significant in these areas, and the coefficient of determination for each fit is still high ($R^2_{min} > 0.977$), and so it is not expected that these details would adversely affect the dynamics of the adsorbate in a meaningful way. The convergence data shows that the spring constant is converged with a 16x16 grid and this interpolated surface is presented in figure 15.

The key advantage of this PES is the speed of MD simulations using it. With the rigorous convergence of the DFT calculations as described above, where each DFT calculation has sub-meV accuracy, it typically takes 2-3 minutes to do a single energy calculation using CASTEP on 144 cores of the UK national supercomputer ARCHER. By comparison, using the triple Fourier interpolated PES, it is possible to do around 2000 MD steps per second on a single core desktop PC. This equates to $\sim 6 \times 10^7$ speed up – and with sub-meV accuracy compared to the full DFT calculation. Without this speedup, it would be too computationally expensive to undertake this diffusion study using *ab initio* PACMD.

## Appendix C: Convergence of Molecular Dynamics Calculations

### 1. Convergence of classical MD

The classical MD simulations used the NVT ensemble, with a Langevin thermostat to ensure ergodicity, in order to simulate the diffusion of hydrogen on the predetermined PES. All MD calculations were performed using the authors' own code[38].

The Langevin thermostat[24] is a stochastic thermostat, based on the Langevin equation[41,42] and the fluctuation-dissipation principle. It is implemented in MD by modifying the force on each particle (at every timestep):

$$\mathbf{F}_i(t) \rightarrow \mathbf{F}_i(t) - \frac{m_i \mathbf{v}_i(t)}{\tau} + \mathbf{R}_i(t), \tag{C1}$$

with each component of the random force, $\mathbf{R}_i$, given by:

$$R_i^{\alpha}(t) = \sqrt{\frac{2m_i k_B T}{\tau \Delta t}} N(0,1) = N\left(0, \frac{2m_i k_B T}{\tau \Delta t}\right), \tag{C2}$$

where $\alpha$ represents one of the Cartesian directions, $\Delta t$ is the time step, and $N\left(\mu, \sigma^2\right)$ is Gaussian random number with a mean of $\mu$ and a variance of $\sigma^2$. As the Langevin force is non-conservative, it follows that the dynamics are no longer Hamiltonian.

The Langevin damping time, $\tau$, controls the coupling of the system to the heat bath. As $\tau \rightarrow 0$, the stochastic term in the thermostat dominates, and the dynamics produced are effectively Brownian motion, and so the $\tau$ should ideally be chosen to be longer than the dominant vibrational period of the system. Here, we are interested in the long time dynamics in order to study diffusion. For the classical test system of a Lennard-Jones liquid[43,44], the effect of $\tau$ on the diffusion coefficient has already been demonstrated[45].

To accurately model the diffusive behaviour of an adsorbate moving across the *static* PES, $\tau$ must be sufficiently long to provide only gentle thermostatting so that the dynamics are approximately NVE-like on timescales of the diffusion. Whilst in reality there will be energy transfer between the surface and the adsorbate, the thermostatting procedure here exists to generate the *average* diffusion rate of the adsorbate between kinetic energy exchange events (collisions) with the surface atoms. To determine how long $\tau$ should be, a series of MD simulations were carried out on the static PES, for both hydrogen and deuterium, with $\tau$ varying from 5 fs to 25000 fs. The diffusion coefficient is calculated from the gradient of the lines of best fit to the time origin averaged mean-squared displacement (RHS of equation 4). To calculate the diffusion coefficient for each value of $\tau$, a timestep of 1 fs was used to generate a total simulation time of 10 ns, with an equilibration time of 0.5 ns. From the remaining 9.5 ns trajectory, the MSD was calculated over segments of 0.95 ns and then time-origin averaging was used to produce a single MSD with improved, and this was then averaged over 10 independent trajectories for each value of $\tau$ to get the final MSD value.

At a high temperature (250 K), the diffusion rates as shown in figure 16 are as expected: the hydrogen is consistently more mobile than deuterium, with a diffusion rate which appears to increase with respect to the damping time (from 5 fs to 100 fs), but is then converged for all values of $\tau \geq 200$ fs. Note that the error in the diffusion coefficient tends to increase as the damping time increases. This is because the run time is fixed at 10 ns, and $\tau$ can be thought of as being the average time between significant thermal "kicks" – which are necessary for the thermostat to operate effectively – and hence very large values of $\tau$ ought to only be used with very long run times in order to get good statistics from the stochastic part of the thermostat. Fortunately, it appears that very large values of $\tau$ are not required.

At low temperatures (250 K), the diffusion is significantly reduced (by 6 orders of magnitude) as can be seen in figure 17. Now there is a marked dependence of the diffusion coefficient on $\tau$ for all values considered, and there is no longer a clear difference between hydrogen and deuterium diffusion.

This strongly suggests that classical diffusion at low temperatures should be considered as a 'rare event' and hence the error in direct MD simulation is relatively large unless prohibitively long run times are used – or alternative 'rare event' approaches should be used instead. With that caveat, it was decided to use $\tau = 500$ fs as a reasonable value across the temperature range.

To determine the temperature dependence of the diffusion rate, 20 independent trajectories (for both hydrogen and deuterium) at 8 different temperatures, were calculated, using the same parameters as the previous calculations (timestep of 1 fs, total time of 10 ns, discarding first 0.5 ns of each trajectory, using time-origin averaging and a Langevin damping time of 500 fs). The resulting diffusion coefficients are presented as a function of the temperature in figure 18.

### 2. Convergence of PIMD

It is important to converge any PIMD calculation with respect to the number of beads, with more beads necessary at lower temperatures. A direct convergence test of the diffusion coefficient with respect to the number of beads is computationally expensive, and so the radius of gyration was used instead as a proxy for delocalisation and other quantum properties. The radius of gyration is a simple measure of the spread of the ring polymer:

$$r = \sqrt{\frac{1}{P}\left\langle \sum_{s=1}^{P} \left(\mathbf{r}_s - \mathbf{r}_c\right)^2 \right\rangle}, \tag{C3}$$

where $\mathbf{r}_c$ is the position of the centroid of the ring polymer and the average is conducted over the length of a trajectory. In anisotropic situations it may also be useful to monitor the full gyration tensor :

$$R^2_{\alpha\beta} = \frac{1}{P}\left\langle \sum_{s=1}^{P} \left(r_s^\alpha - r_c^\alpha\right)\left(r_s^\beta - r_c^\beta\right) \right\rangle, \tag{C4}$$

where $\alpha$ and $\beta$ are the Cartesian components. The radius of gyration can also be computed from the trace of the gyration tensor.

For the following convergence calculations, conventional PIMD (not PACMD) simulations of H and D at 75 K and 250 K were carried out for a varying number of beads (from 2 to 64), each for a total run time of 2.5 ns, with a timestep of 1 fs. The previous classical MD simulations are equivalent to a 1 bead PIMD calculation, and so the same Langevin damping time of 500 fs can be used here as well. All PIMD calculations were performed using the authors' own code[38].

Figure 19 shows the mean radius of gyration and virial total energies as a function of the number of beads. We see the expected behaviour: at convergence, H is more delocalised (has a larger radius of gyration) than D at the same temperature, and the radius of gyration for both particles is larger at lower temperatures — indicating that delocalisation will play more of a role at lower temperatures. In addition, the virial total energies are also what we would expect — larger for H than D at the same temperature (increased zero point energy), and both increase as the temperature increases. For our calculations, 16 beads were chosen to represent the quantum particle — although it may be argued that 32 beads may be required for H at 75 K, it was not felt that this warranted a doubling in the computational cost for such a small apparent gain.

### 3. Convergence of PACMD

The additional convergence parameter for PACMD is the adiabaticity parameter, $\gamma$, which needs to be reduced until the diffusion coefficient is converged. Unfortunately, as $\gamma$ decreases, the computational cost associated with these simulations tends to increase as the time step must also decrease in order to accurately simulate the dynamics of the (increasingly light) non-centroid modes. A direct convergence test of the diffusion coefficient with respect to $\gamma$ is therefore very expensive and so we again use other parameters as a proxy. If $\gamma$ is smaller than necessary then it should not adversely affect the diffusion rates, but it will increase computational cost due to the smaller time step. Hence we must first determine the timestep required for the smallest $\gamma$ before we can find the optimal value of $\gamma$. Testing showed that the largest timestep which could be used for our lower bound of $\gamma = 0.0025$ was found to be 0.005 fs — even a timestep as small as 0.01 fs was found to produce unstable dynamics at 250 K for H (although D at 250 K was stable with this timestep) — as was evident by a discontinuous jump in the radius of gyration during a simulation.

Once the optimal timestep was set, a series of PACMD calculations were carried out to determine which value of $\gamma$ was required to accurately converge the centroid force, and therefore correctly calculate the quantum dynamcs. For this process, various measures were tested, and it was found that the most reliable were the variance in the radius of gyration and in the virial total energy. In all cases there was a clear tendency for fluctuations to become smaller as the adiabaticity parameter decreased. This suggested that there becomes a point when the masses of the non-centroid modes are sufficiently small to give rise to oscillations about the centroid which are relatively unaffected by a change in their position across the PES. The results of figure 20 suggests that $0.0025 \leq \gamma \leq 0.025$ for convergence. These calculations were carried out for a range $\gamma$ (from 0.0025 to 0.75), for both H and D at high (250 K) and low (75 K) temperatures, for a total simulation time of 250 ps, again with a Langevin damping time of 500 fs. All PACMD calculations were performed using the authors' own code[38].

The fluctuations of the virial total energy in NVT PIMD are analagous to the fluctuations in the Hamiltonian in NVE classical MD, and so these fluctuations represent a measure of the quality of the integration of the adiabatically averaged equations of motion of the centroid in PACMD. Hence reduced fluctuations in the virial total energy implies a reduction in the error in the calculation of the centroid mean force. Figure 21 suggests that all values of $\gamma \leq 0.1$ are suitable for accurate integration of the centroid equations of motion.

On the basis of the results presented in figures 20 and 21, we chose an adiabaticity parameter of $\gamma = 0.01$ for the quantum diffusion simulations. Whilst this is not full adiabatic separation, the results of Hone *et al*[25] have shown that it is not completely necessary to guarantee a *complete* adiabatic separation between the centroid and non-centroid modes in order to accurately determine time correlation functions — in fact, it is precisely this result which allows for the PACMD method to be more efficient than fully adiabatic centroid MD. With this value of $\gamma$ we were able to increase the timestep from 0.005 fs (necessary for $\gamma = 0.0025$ ) to 0.05 fs. If the timestep is made larger then the radius of gyration again exhibits a discontinuous jump in the output for H at 250 K.

Finally, figure 22 shows the diffusion coefficient as a function of temperature, resulting from an averaging over each of the 12 independent runs at each temperature. Although the curve is less smooth than the classical calculations, the diffusion rates span fewer orders of magnitude across the temperature range being studied than in the classical simulations. In addition, even at the highest temperature studied throughout this work (250 K), quantum effects act to increase the diffusion rate significantly for both hydrogen and deuterium.

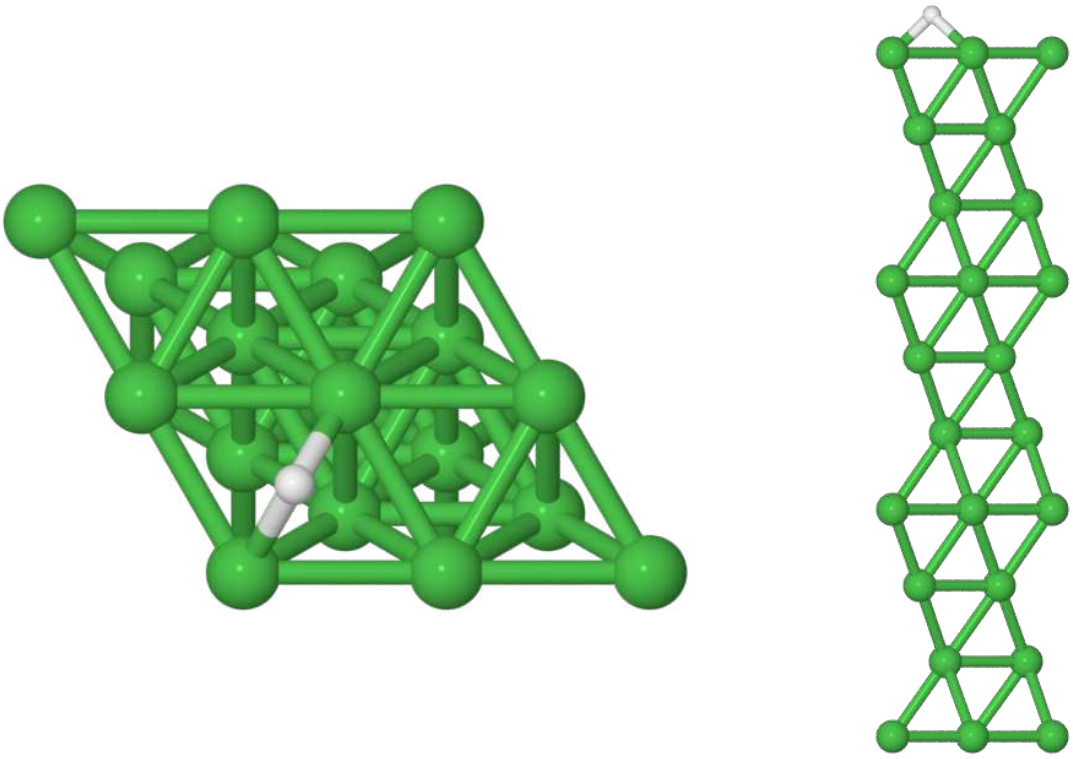

Figure 1: (Colour online) Top and side view of the nickel slab used for the DFT PES calculations. Due to the symmetry of the slab, the H atom is only scanned across sites in the irreducible wedge of the (111) surface.

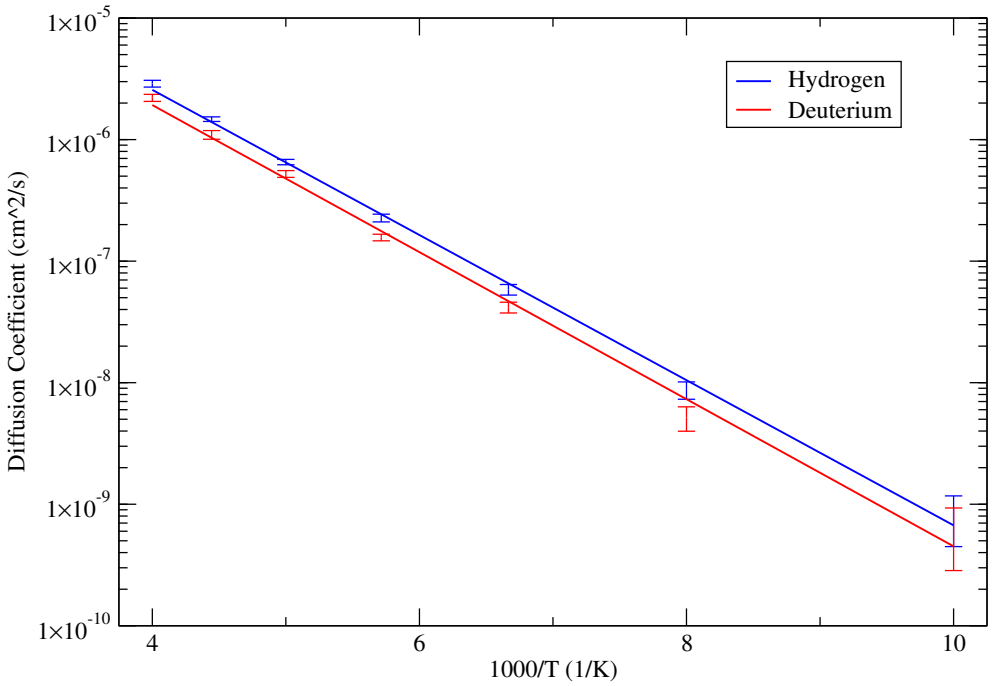


Figure 2: (Colour online) Arrhenius plot of the diffusion coefficient as a function of inverse temperature, for classical simulations of H and D on the Ni(111) surface (shown with lines of best fit).

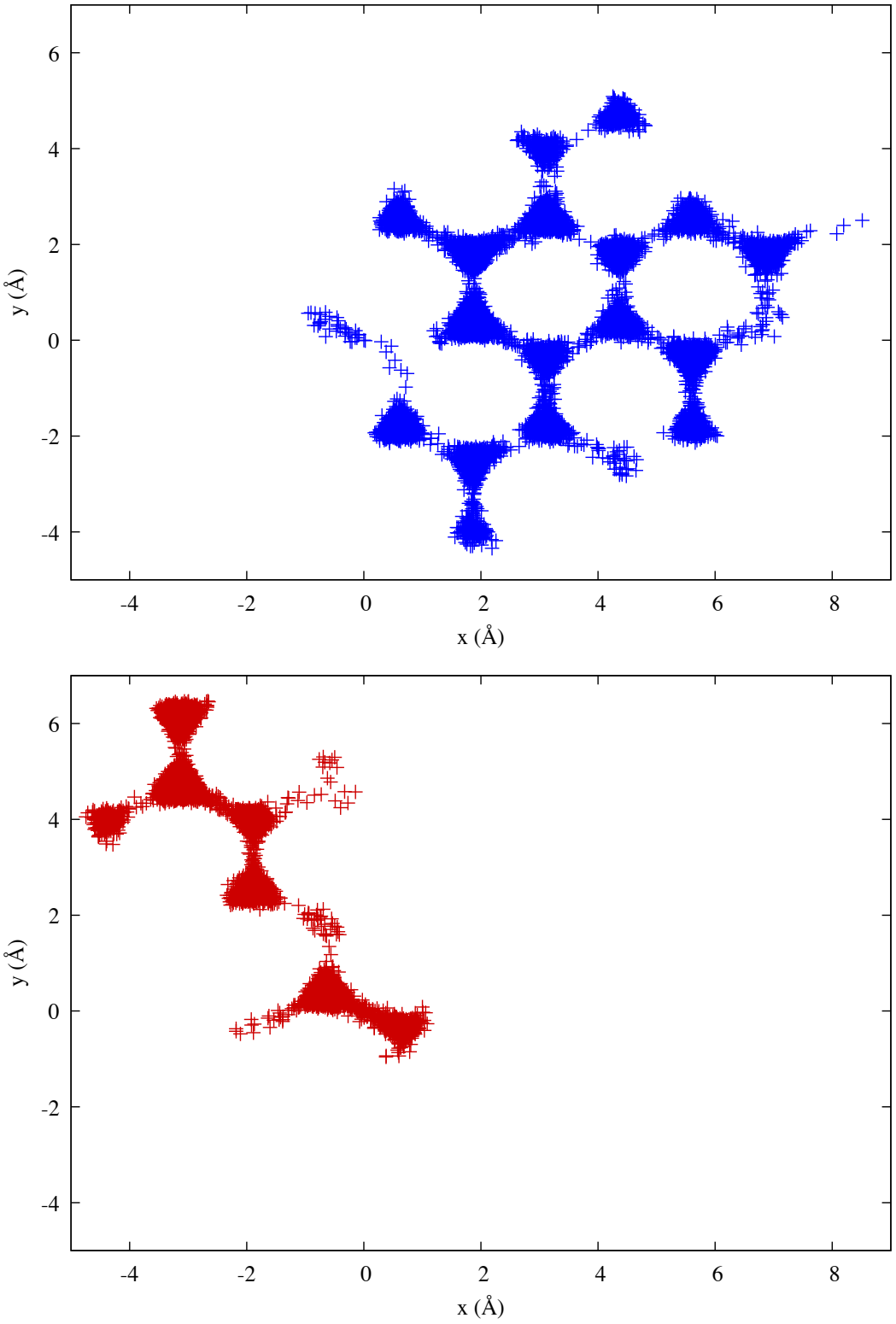


Figure 3: (Colour online) The trajectories of H (top, blue) and D (bottom, red) across the Ni(111) PES at a temperature of 250 K. For visualisation purposes, these trajectories were plotted from a short 500 ps simulation. All other simulation parameters were kept the same.

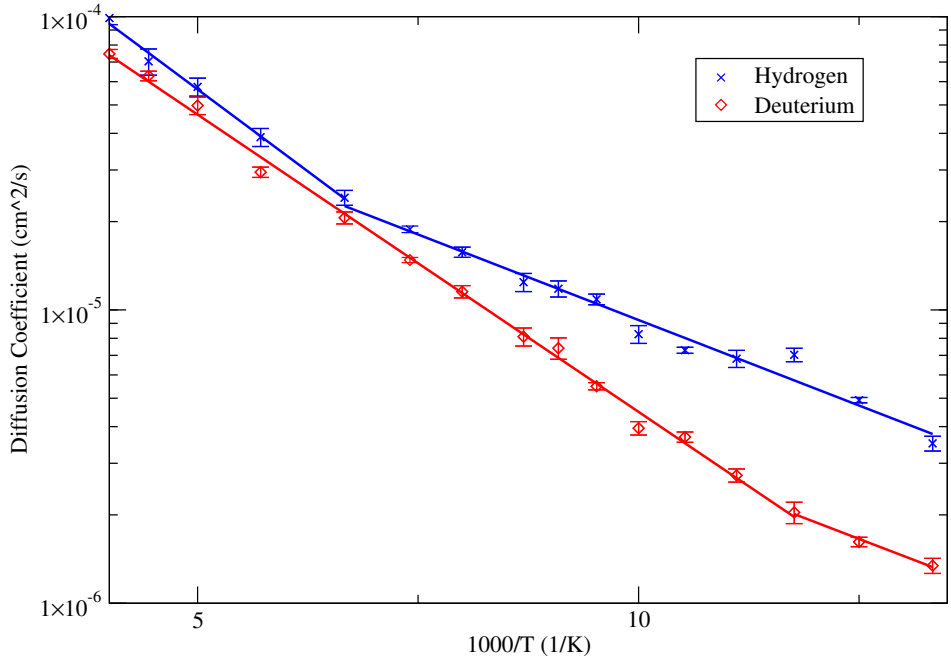


Figure 4: (Colour online) Arrhenius plot of diffusion rates against inverse temperature from PACMD simulations of H and D on the Ni(111) surface (using 16 beads). The H data shows a sharp change in the slope which indicates a transition from classical to quantum diffusion and so the data is plotted with two lines of best fit, corresponding to high temperatures (from 250 K to 150 K), and low temperatures (150 K to 75 K). The corresponding transition temperature for D is approximately 85 K as shown.

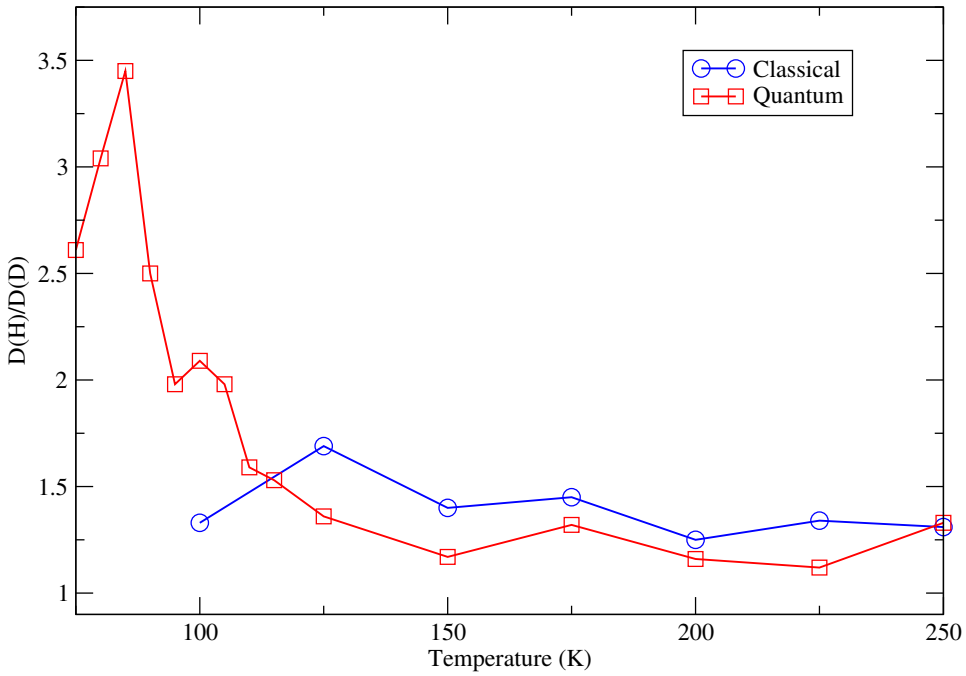


Figure 5: (Colour online) The ratio of H to D diffusion coefficients for classical and quantum (PACMD, 16 beads) simulations on the Ni(111) surface as a function of temperature.

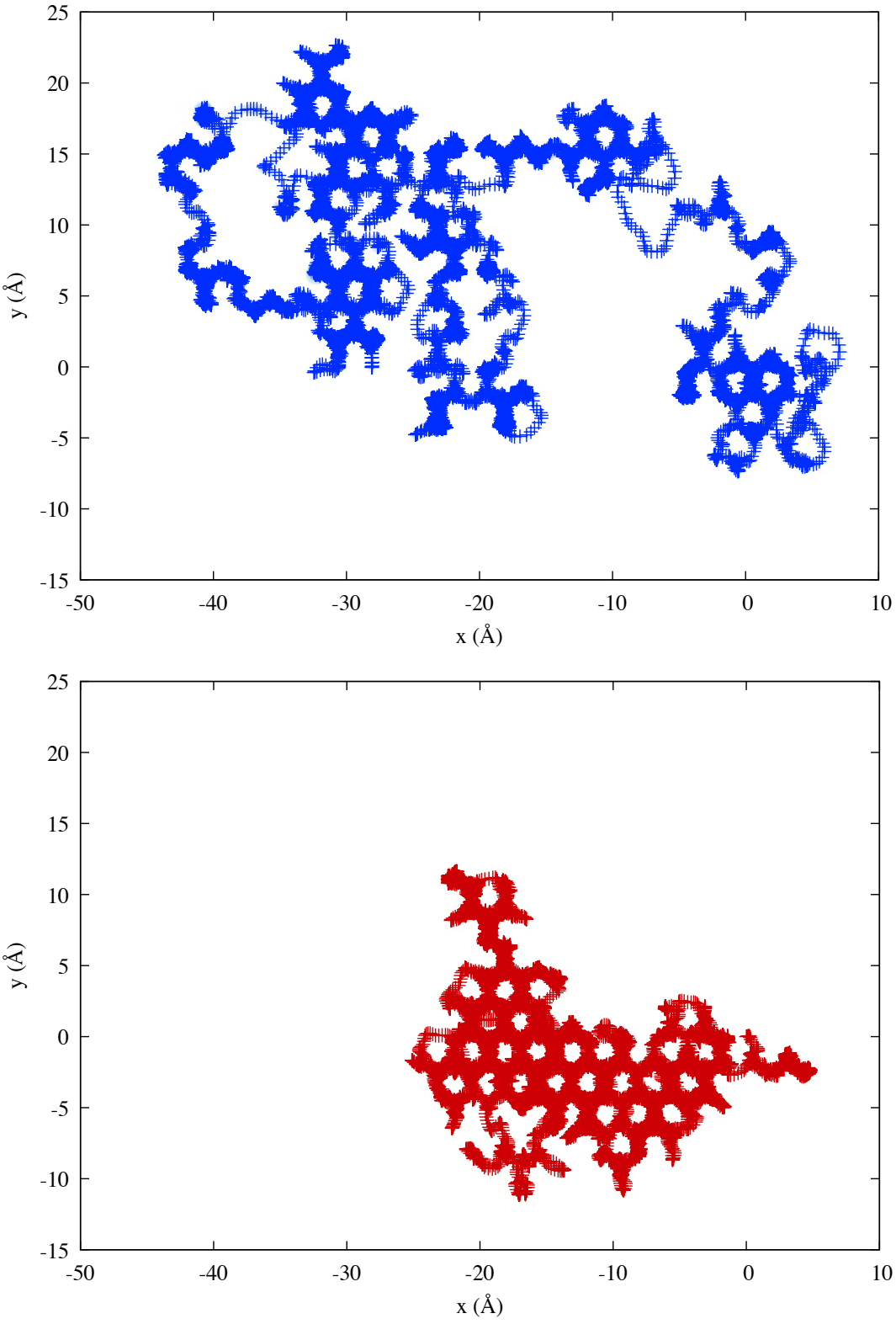


Figure 6: (Colour online) Quantum trajectories of the H (top, blue) and D (bottom, red), both represented by a ring polymer (of 16 beads), across the Ni(111) PES at a temperature of 250 K. These plots were generated from a short PACMD trajectory of 200 ps. All other simulation parameters were kept identical to those used for the calculation of the diffusion coefficients (16 beads, Langevin damping time of 500 fs and an adiabaticity parameter of 0.01). Here the (darker) points represent the centroid position, with the (lighter) circles representing the radius of gyration of the ring polymer at that point.

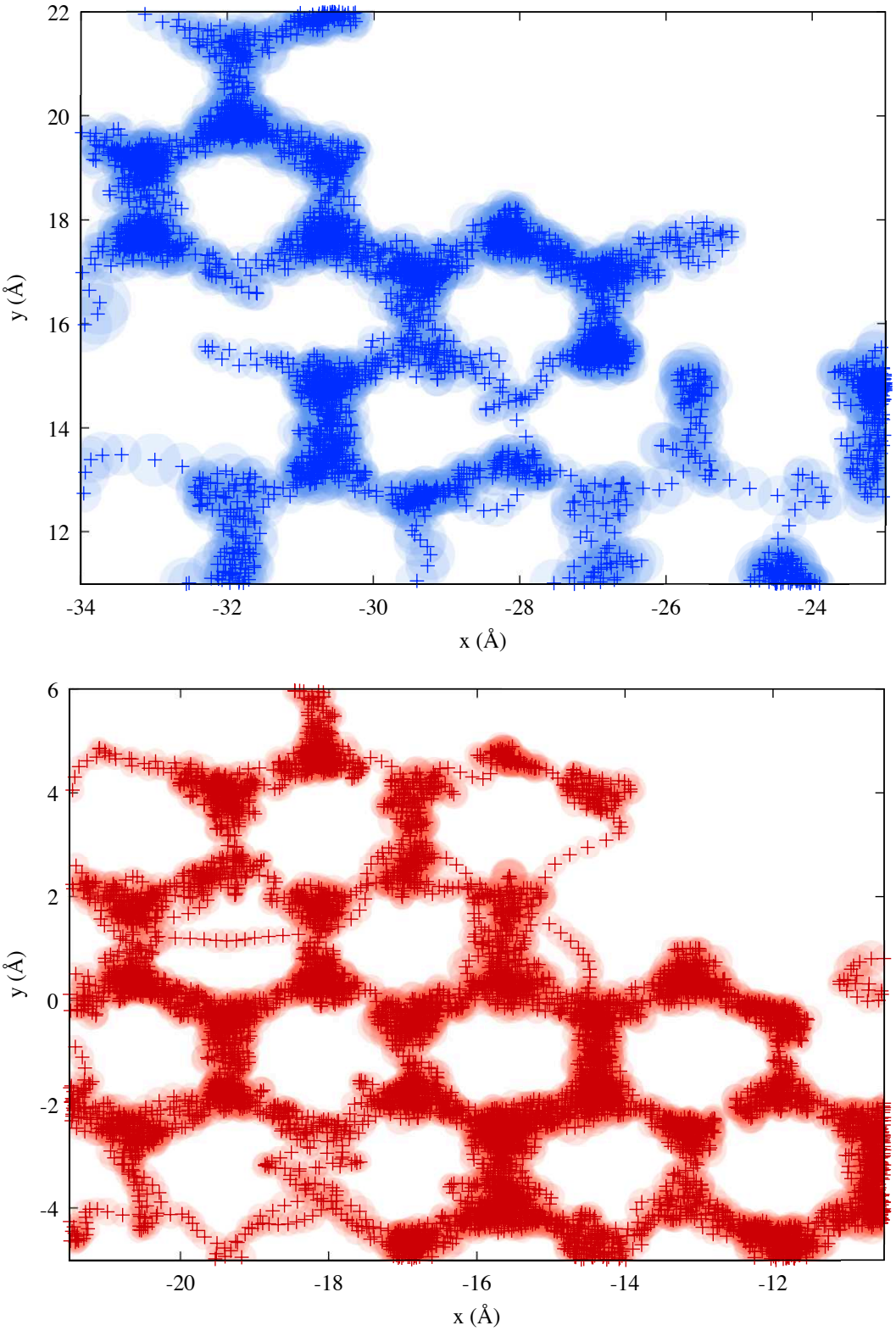


Figure 7: (Colour online) A subset of the quantum trajectories shown in figure 6 for H (top, blue) and D (bottom, red) moving across the Ni(111) PES at 250 K.

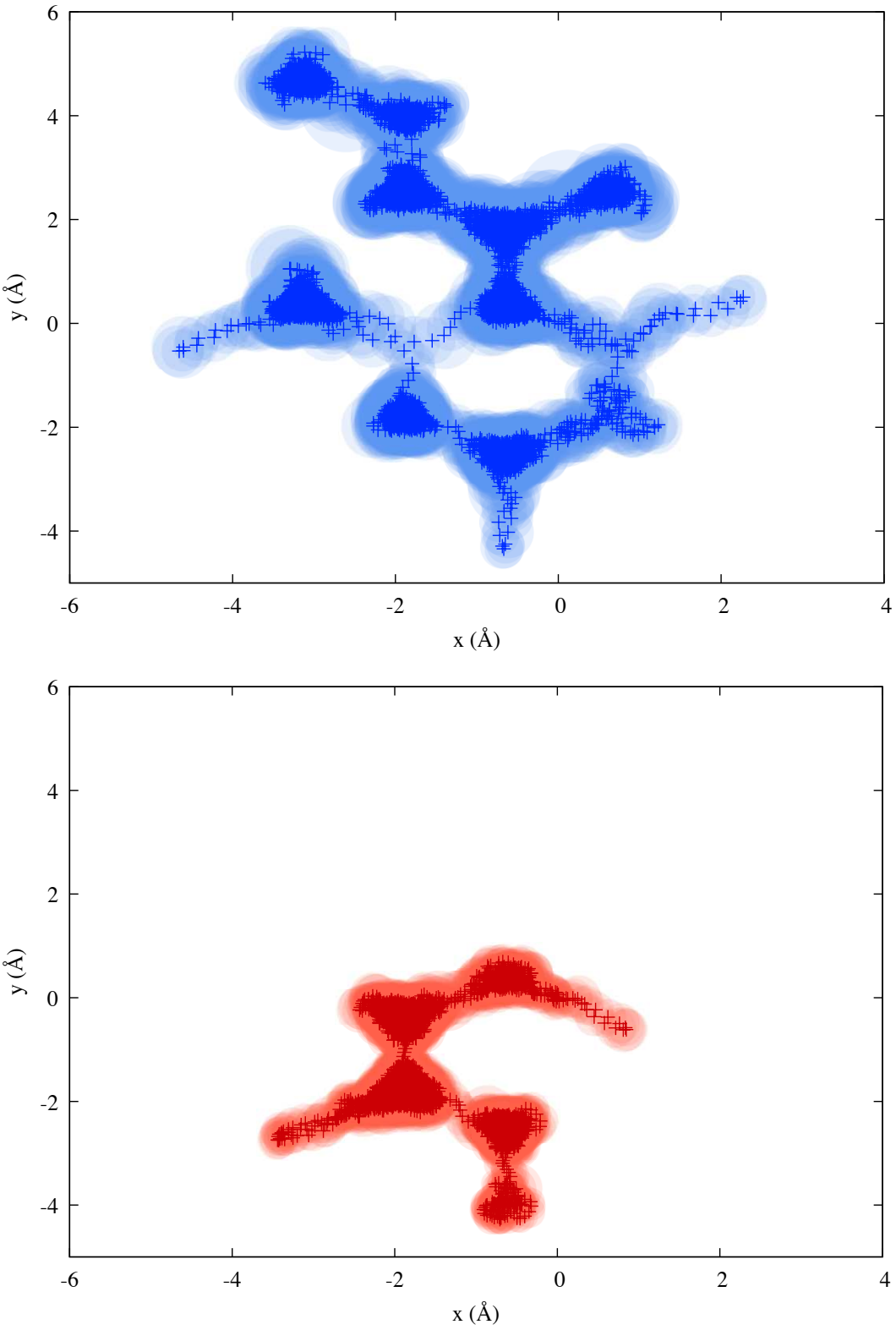


Figure 8: (Colour online) Quantum trajectories of the H (top, blue) and D (bottom, red), both represented by a ring polymer (of 16 beads), across the Ni (111) PES at a temperature of 75 K. These plots were generated from a short PACMD trajectory of 200 ps. All other simulation parameters were kept identical to those used for the calculation of the diffusion coefficients (16 beads, Langevin damping time of 500 fs and an adiabaticity parameter of 0.01). Here the (darker) points represent the centroid position, with the (lighter) circles representing the radius of gyration of the ring polymer at that point.

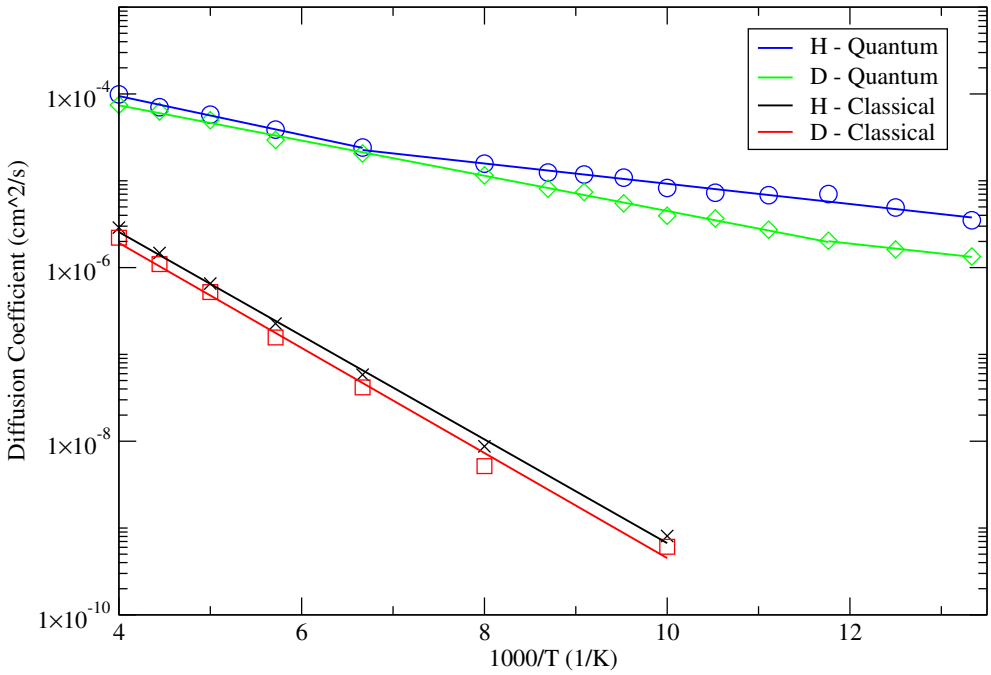


Figure 9: (Colour online) Arrhenius plots of the diffusion coefficient as a function of inverse temperature for classical and quantum (PACMD, 16 beads) of H and D on the Ni(111) surface. Presented with lines of best fit (1 line for classical results, 2 lines for quantum results).

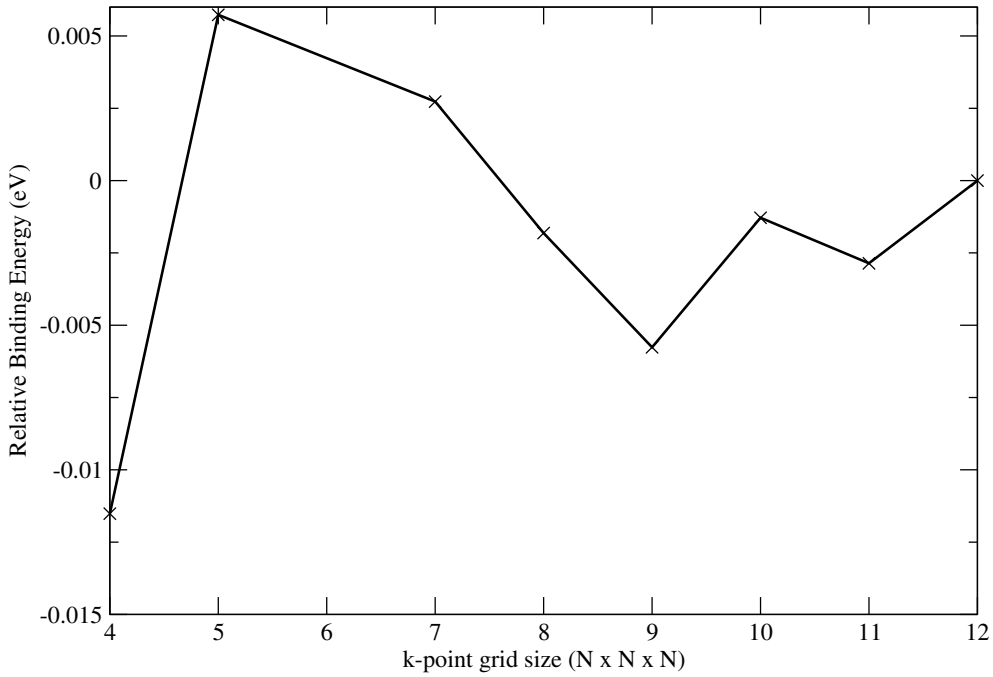


Figure 10: Change in binding energy for a hydrogen atom placed in a bulk nickel system (with a 400 eV cut-off energy) as a function of **k**-point grid size. The convergence of binding energy is not monotonic as **k**-point grid dimensions are increased: the zero of energy is defined for 12x12x12 **k**-point grid. For a 7x7x7 grid, the energy difference is 2.7 meV.

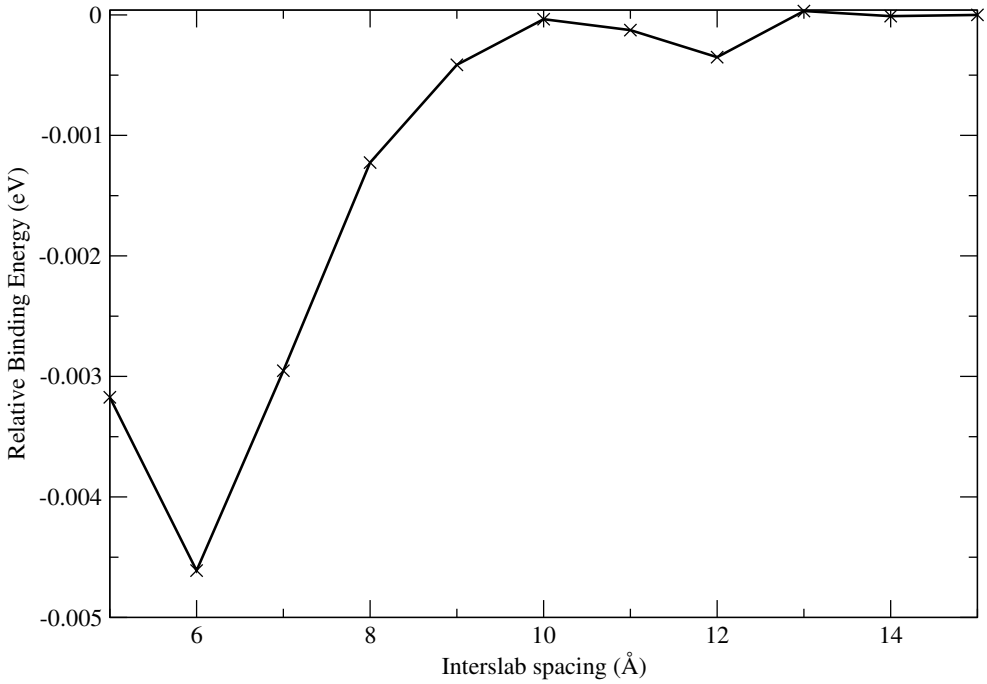


Figure 11: Convergence of binding energy for a hydrogen atom placed 1.5 Å above a 4 layer thick (111) nickel surface as a function of inter-slab spacing. The zero of energy is defined for a 15 Å spacing between neighbouring slabs. At 10 Å, the change in energy is less than 0.04 meV – this corresponds to a vacuum gap of 8.5 Å above the H atom.

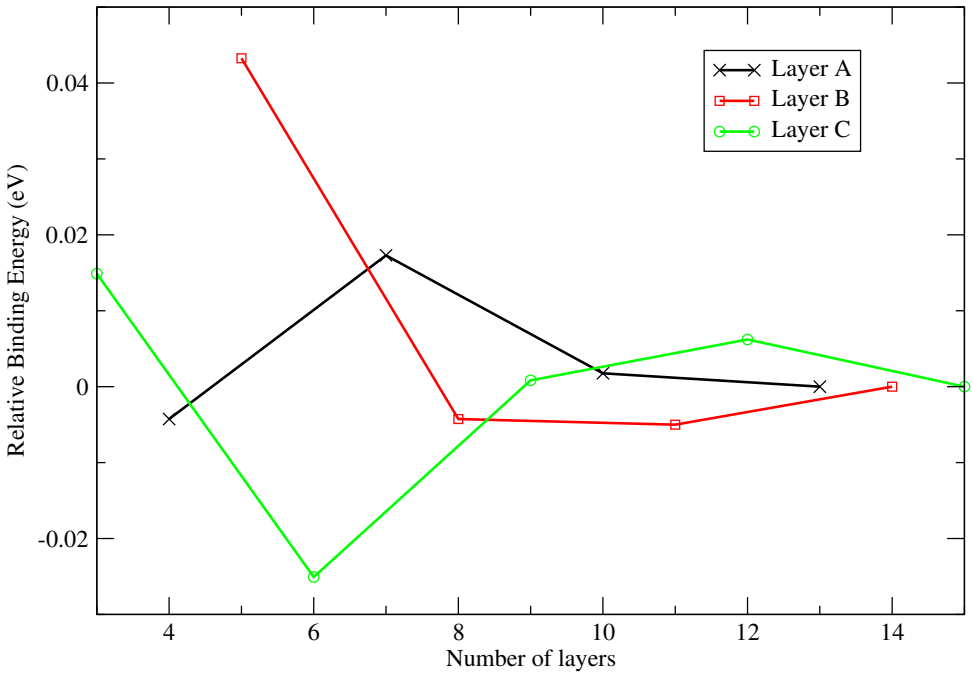


Figure 12: (Colour online) Convergence of binding energy as a function of number of layers, for a hydrogen atom placed 1.5 Å above a nickel (111) surface, with an inter-slab spacing of 6 Å (4.5 Å of vacuum above the H). The cut-off energy was 725 eV, and the **k**-point grid was 7x7x1. For 10 layers, the change in binding energy reduces to 1.8 meV. The layer labelling refers to label of the top-most nickel layer, where the bottom layer is always layer "A". The hydrogen atom binds to the top-most nickel layer.

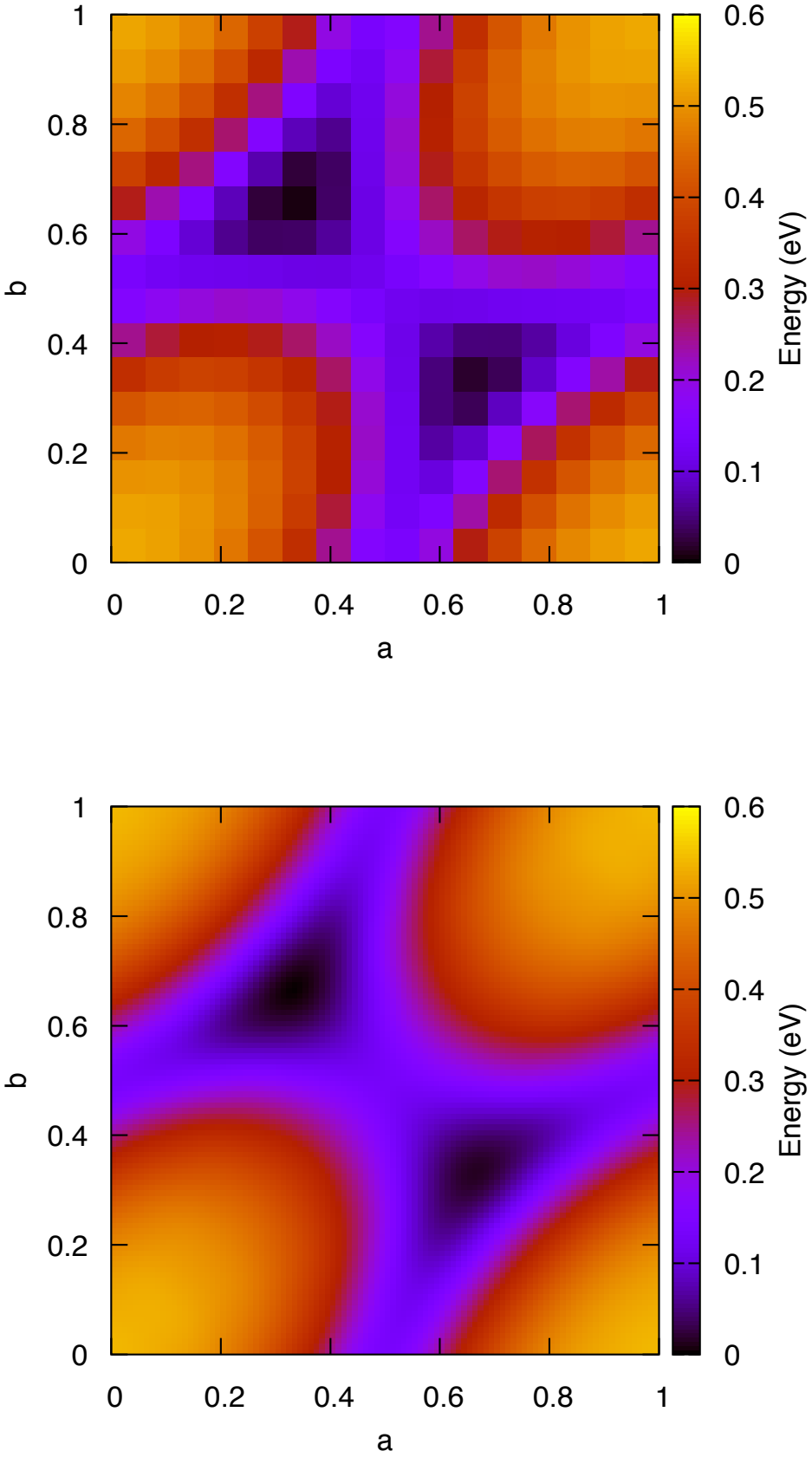


Figure 13: (Colour online) Relative potential energies of a single H atom, interacting with a 2x2 Ni(111) surface, calculated using DFT. The raw data (upper) and the interpolated surface (lower) are presented for a 16x16 grid. All energies are shown relative to the global minimum.

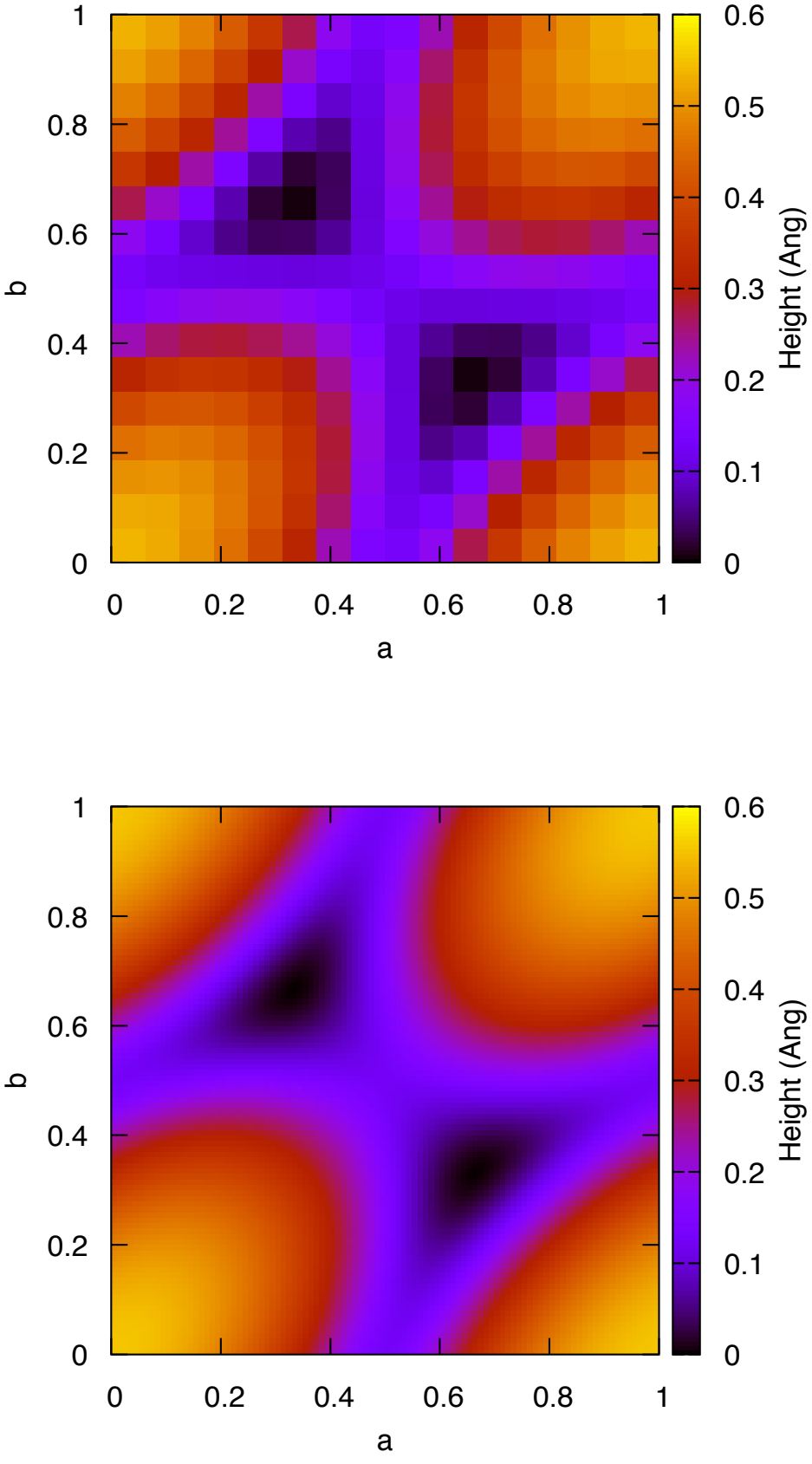


Figure 14: (Colour online) Relative binding heights of a single H atom, interacting with a 2x2 Ni(111) surface, calculated using DFT. The raw data (upper) and the interpolated surface (lower) are presented for a 16x16 grid. All heights are shown relative to the global minimum.

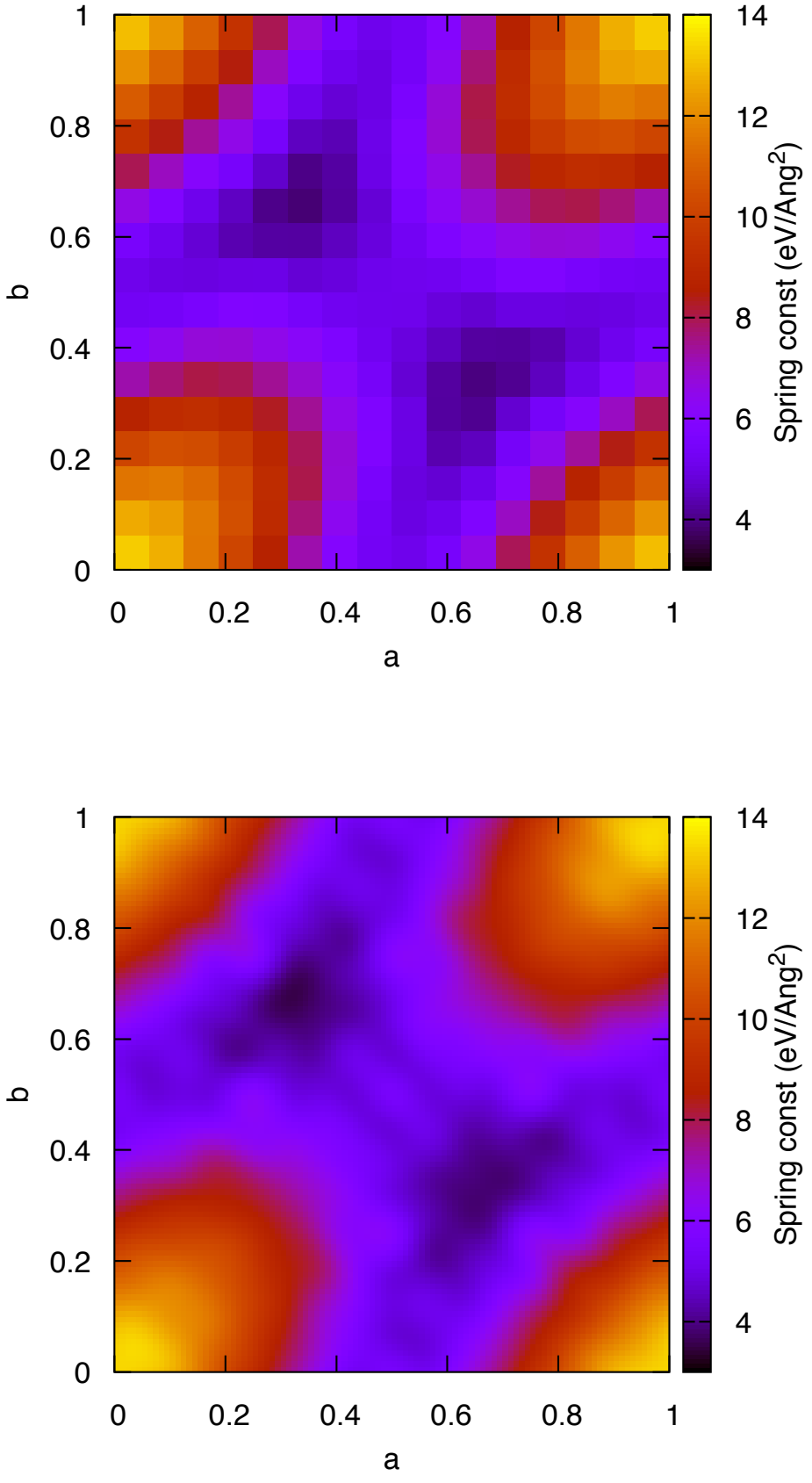


Figure 15: (Colour online) Effective spring constants approximating the **c**-dependent harmonic interaction for a single H atom, interacting with a 2x2 Ni(111) surface, calculated using DFT. The raw data (upper) and the interpolated surface (lower) are presented for a 16x16 grid.

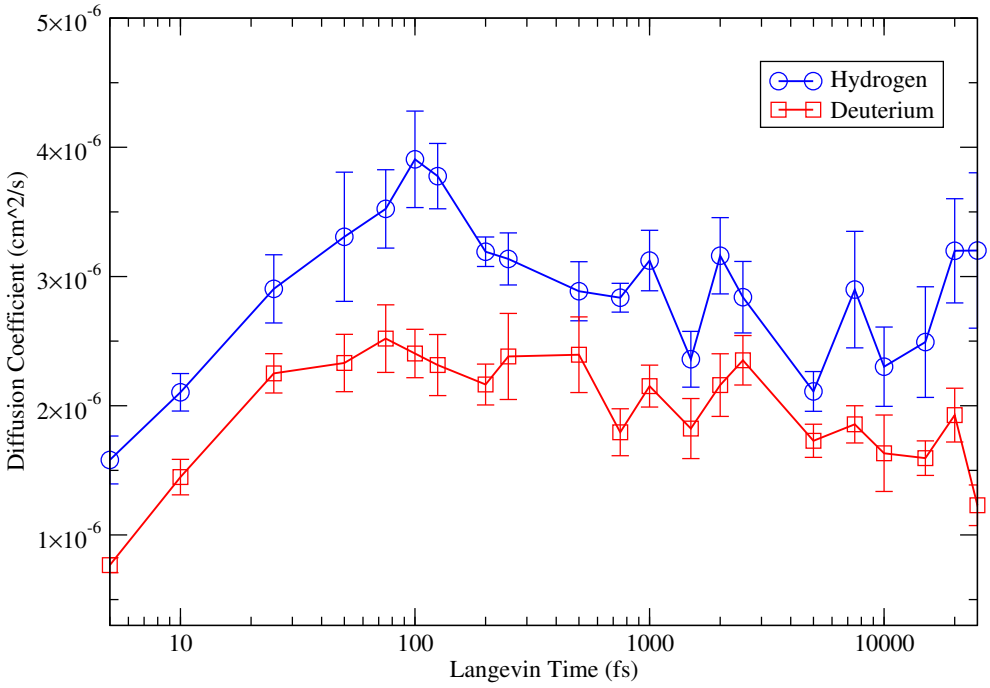


Figure 16: (Colour online) Diffusion coefficients of classical H and D on the Ni(111) surface, as a function of the Langevin damping time, at a temperature of 250 K.

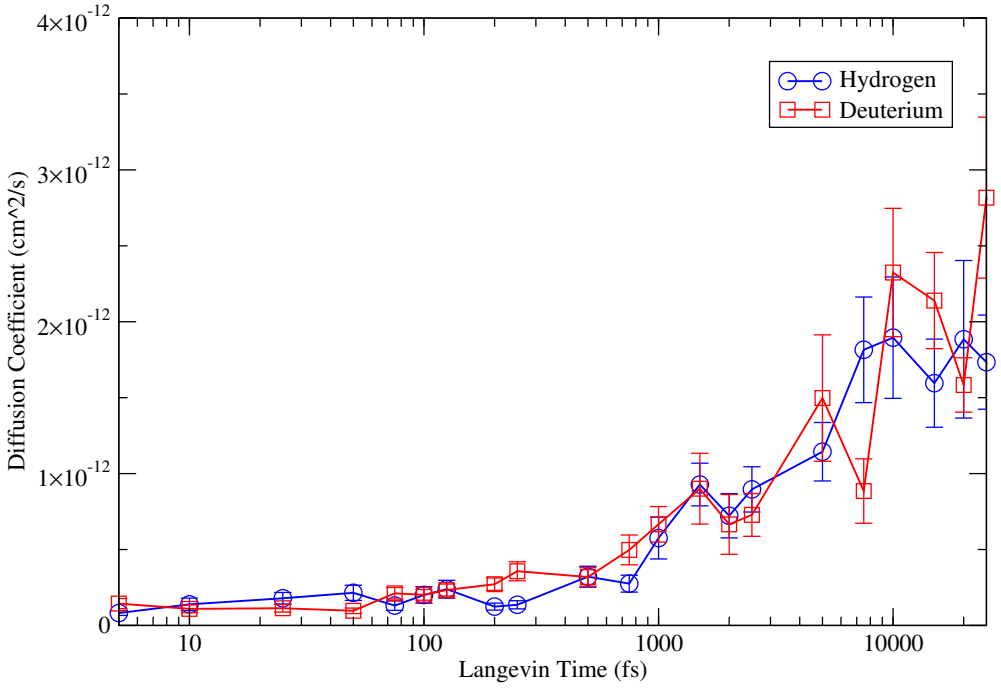


Figure 17: (Colour online) Diffusion coefficients of classical H and D on the Ni(111) surface, as a function of the Langevin damping time, at a temperature of 75 K.

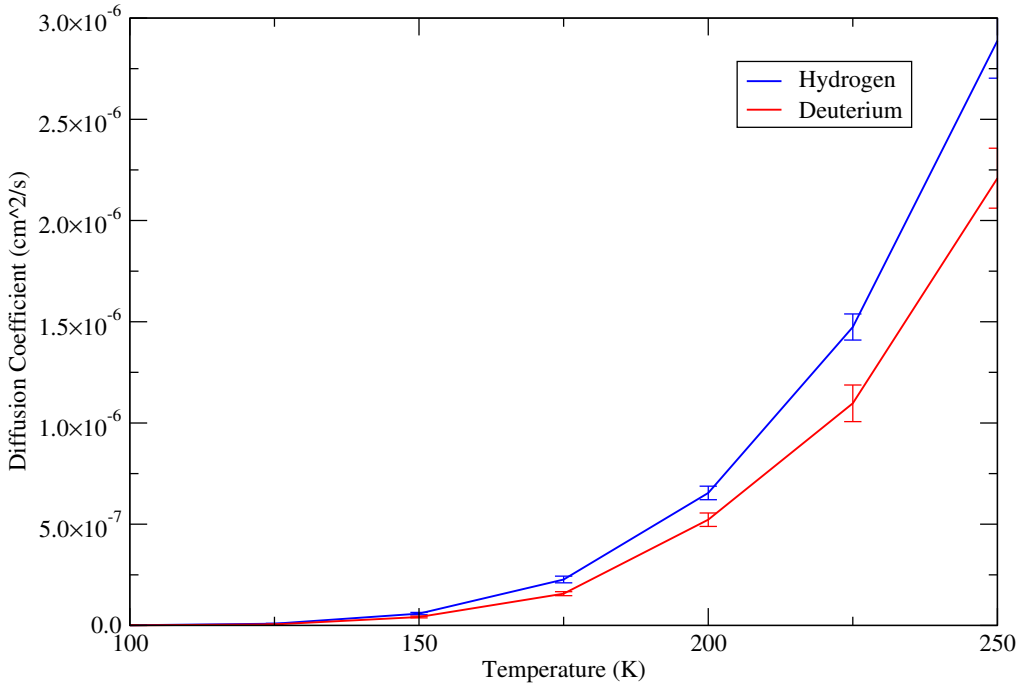


Figure 18: (Colour online) Diffusion coefficients as a function of temperature for classical simulations of H and D on the Ni(111) surface.

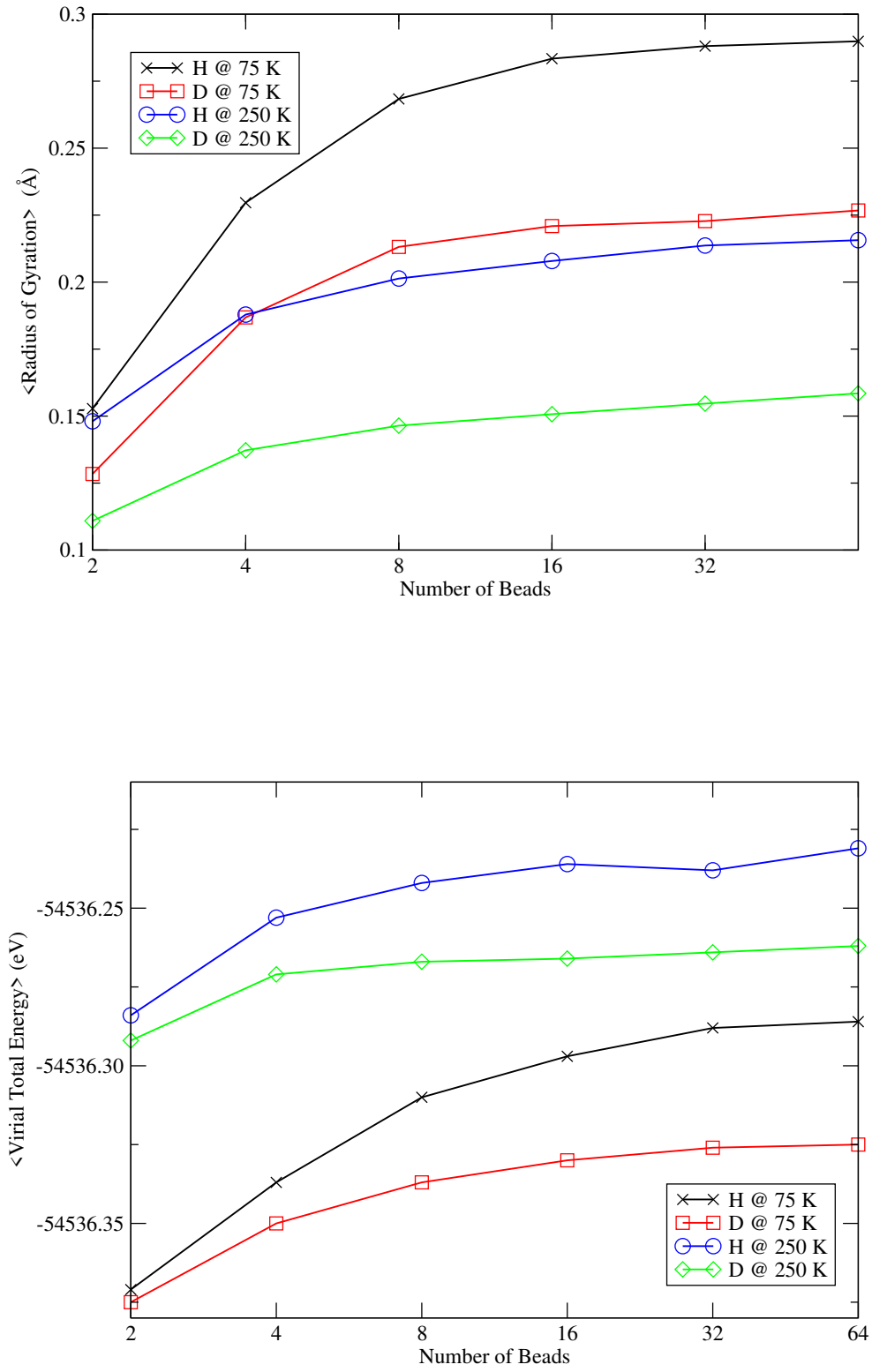


Figure 19: (Colour online) Convergence behaviour of the mean radius of gyration (top) and virial total energy (bottom) as a function of the number of beads, for H/D on Ni(111) at 75 and 250 K.

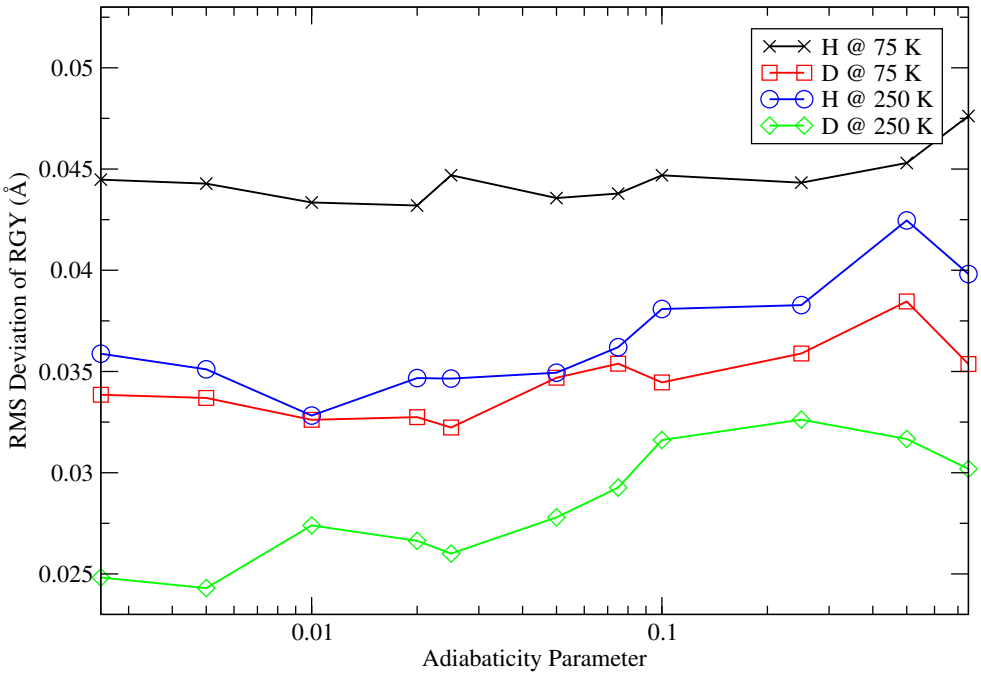


Figure 20: (Colour online) The root mean squared fluctuation of the radius of gyration of H (top) and D (bottom) on the Ni(111) surface, at 75 K and 250 K, for varying amounts of adiabatic separation between the centroid and non-centroid modes (16 beads).

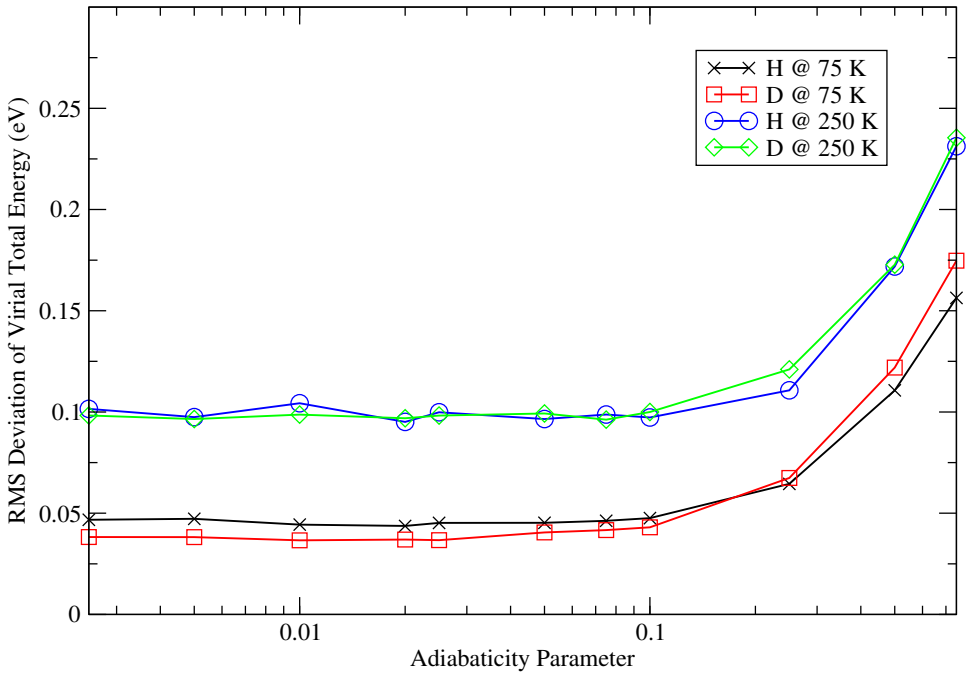


Figure 21: (Colour online) The root mean squared fluctuation of the virial total energy estimator for H and D on the Ni(111) surface, at 75 K and 250 K, as a function of the adiabaticity parameter (16 beads).

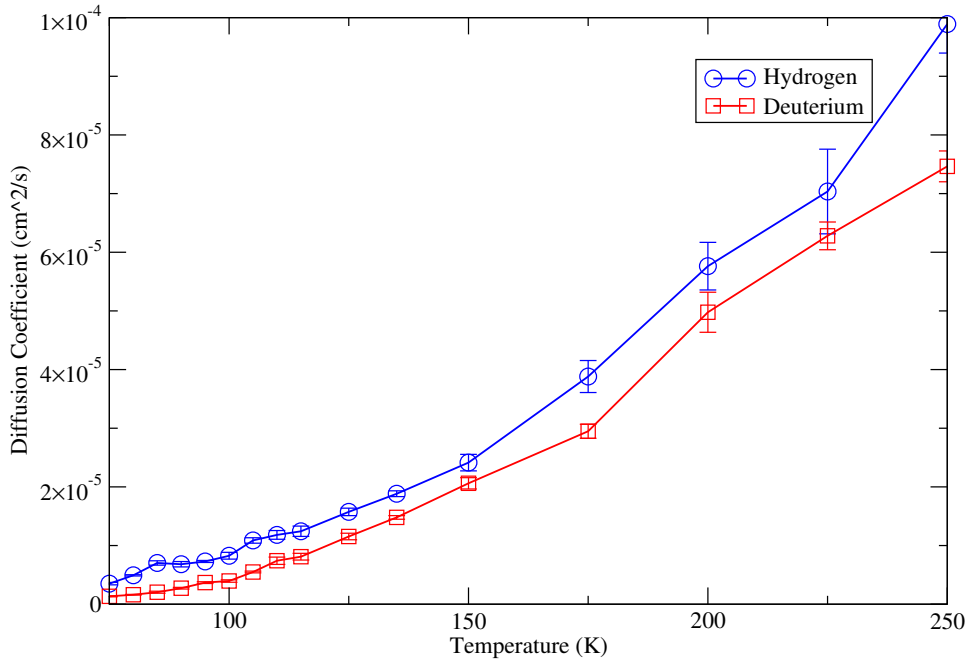


Figure 22: Diffusion coefficient as a function of temperature for quantum (PACMD) simulations of H and D on the Ni(111) surface (using 16 beads).